PHOSPHORUS–BASED NEGATIVE ELECTRODES FOR SODIUM-ION BATTERIES

by

Lituo Zheng

Submitted in partial fulfilment of the requirements
for the degree of Master of Science

at

Dalhousie University
Halifax, Nova Scotia
January 2016

TABLE OF CONTENTS

LIST OF TABLES

LIST OF FIGURES

ABSTRACT

Sodium ion batteries are promising for future use in electrified vehicles and electrical power grids. However, there exist many challenges in the development of negative electrode materials. In this work, room temperature ^{119}Sn Mössbauer spectroscopy and X-ray diffraction were used to study the sodiation mechanism of Sn_4P_3. The results suggest that upon sodiation, Sn and P begin to react with sodium simultaneously and different Na-Sn phases were formed. These findings are consistent with the behavior of Sn_4P_3 in Li cells. This study provides an example of how Mössbauer spectroscopy can provide insight into the mechanism of metal alloying reactions in metal ion cells. Five transition metal phosphides (M-P, M=Ti, Mn, Co, Cu, Zn) were synthesized and tested in sodium ion half-cell for use as negative electrode materials. The possibility of using transition metal phosphides as negative electrode was evaluated. Conversion reactions occur during the sodiation/desodiation of the materials. It was found that even though some transition metal phosphides offer high capacities, they all suffer from high irreversible capacity, poor cycling life and high voltage hysteresis. The effects of using different binders and operating temperatures were also explored.

LIST OF ABBREVIATIONS USED

LCO	Lithium cobalt oxide
NMC	Lithium nickel manganese cobalt oxide
NCA	Lithium nickel cobalt aluminum oxide
LFP	Lithium iron phosphate
SEI	Solid electrolyte interphase
EC	Ethylene carbonate
CMC	Carboxymethyl cellulose
PVDF	Poly(vinylidene fluoride)
PAA	Polyacrylic acid
FEC	Fluorinated ethylene carbonate
XRD	X-ray diffraction
$\Delta(CS)$	Center shift
PI	Polyimide
NMP	N-methyl-2-pyrrolidone
BMF	Blown microfiber
DEC	Diethyl carbonate
CCCV	Constant current constant voltage
Γ	Full Width Half Maximum Mössbauer Spectrum Peak
Δ	Quadrupole Splitting

ACKNOWLEDGEMENTS

CHAPTER 1   INTRODUCTION

Lithium-ion batteries are now being widely used in portable electronics, such as laptops, cellphones and power tools. Since their first introduction to the market in the early 1990's, lithium-ion batteries have greatly changed people's lifestyle. During the last few years, highway-capable electric vehicles powered by lithium-ion batteries were commercialized by companies including Tesla, Nissan, BYD, etc. Electric vehicles reduce the consumption and dependence on fossil fuels. As of the end of June 2015, the Renault-Nissan Alliance has sold more than 250,000 electric vehicles worldwide. It is anticipated that electric vehicles will gain more market share in the future.[1]

Because of concerns of human impact on the environment, people are developing greener and renewable energy resources, such as wind and solar energy. These natural sources of energy, however, are usually intermittent and unstable. Therefore, large scale energy storage systems are needed. Rechargeable battery technology is promising to play a vital role in electric grid energy storage.[2] Recently, Tesla introduced the Powerwall, a lithium-ion battery product for home use. The Powerwall stores the electricity generated from solar panels. The energy can be used for domestic consumption, load shifting and backup power.[3]

Although lithium ion batteries are efficient, they come with various setbacks. The merits of lithium-ion batteries are high energy density (>700Wh/L), long cycle life (>1000 cycles), high charge/discharge efficiency (>80%) and low maintenance. However, problems in regards to the cost and safety still remain. Today, about one-quarter of world's lithium production is consumed by the manufacturing of lithium batteries,[4] but lithium is not regarded as an abundant element. The abundance of lithium is only about 20 ppm in earth's crust.[5] Lithium is a geographically limited resource; more than half of the lithium reserves on earth are located in South America.[6]

As electric vehicles and electric grid energy storage become popular, the increasing demand for lithium ion batteries could lead to a price rise.

The basic chemistry of modern lithium-ion batteries remains relatively unchanged for about twenty years. The cathode and anode markets are dominated by layered lithium transition metal oxide and graphite, respectively.[7] Significant progresses have been made in the last two decades in regards to cost reduction and energy density improvement of lithium-ion batteries. Most advances come from the modifications of engineering and design of the cell and not of the chemicals used. It is thought that the energy density improvement is approaching the theoretical limit.[8]

Sodium ion batteries are considered to be one of the alternatives to the currently widely-used lithium ion batteries. Compared with lithium, sodium is cheaper and more abundant. Sodium is the sixth most abundant element on earth. Sodium salt is one of the most easily accessible reserves everywhere, as there is a virtually unlimited sodium source in the ocean.[9] In addition, cobalt, which is usually used in the cathodes of most of the current lithium ion batteries, is very expensive and scarce. However, cobalt may not be necessary as a component of cathode materials in sodium ion batteries. This will bring the cost of sodium ion batteries down even more.[10] Moreover, the current collector is a major cost in battery production. Copper is used as current collector of negative electrode in lithium-ion battery production. Sodium does not alloy with aluminum, therefore aluminum could be used as the current collector for negative electrodes instead of more expensive copper.[11] From a chemical perspective, sodium is the second lightest and second smallest alkali metal. It shares the same group with lithium and has many similarities to lithium. The redox potential of sodium (E=-2.71V versus standard hydrogen

electrode) is only ~0.3 V higher than that of lithium. All these features show that sodium-ion batteries have the potential to be a low-cost alternative to lithium-ion batteries.[11]

1.1 MOTIVATIONS

Some promising advances in cathode materials for sodium ion batteries have been made in last two decades. Researchers have shown a number of transition metal oxides[12–14] as well as poly-anionic compounds[15,16] as cathode materials with good capacity and cyclability. However, the lack of appropriate anode materials hinders the development of sodium ion batteries. Like lithium ion batteries, the use of a sodium metal as anode material in sodium ion batteries suffers from poor coulombic efficiency and a severe dendrite problem that can cause safety concerns.[17] Therefore, the development of appropriate anode materials is of great importance in the progress of advancing sodium ion batteries. Graphite is used in most lithium ion batteries as an anode material, however, sodium cannot insert into graphite to any appreciable extent under normal pressure.[18] Even so, carbonaceous anode materials are still appealing for their low cost and availability. Hard carbon has been extensively studied as an anode material for sodium ion batteries. It has a gravimetric capacity of about 300 mAh/g, or a volumetric capacity of about 450 Ah/L.[19,20] In contrast, graphite, the most commonly used anode in lithium ion batteries, has a gravimetric capacity of about 370mAh/g, or a volumetric capacity of about 750 Ah/L. Besides, most of the capacity of hard carbon is at a very low voltage (<0.05 V), which cannot be utilized in a practical cell. This lowers the capacity of hard carbon even more. Hence, the successful commercialization of sodium ion batteries requires a better anode material that is comparable to graphite anode in lithium ion batteries.

There are usually three types of reactions regarding negative electrode materials: alloying reactions, conversion reactions and intercalation reactions. Alloy materials have high energy density and have been proposed to be promising anode materials for sodium ion batteries. Some of the Group 14 and 15 elements can form binary compounds with sodium with a high theoretical volumetric capacity, such as $Na_{3.75}Sn$ (847 mAh/g, 1210 Ah/L, desodiation at ~0.3V)[21] Na_3P (2594 mAh/g, 1401 Ah/L, desodiation at ~0.5V)[22,23], $Na_{3.75}Pb$ (485 mAh/g, 1182 Ah/L, desodiation at ~0.4V)[24], Na_3Bi (385 mAh/g, 1075 Ah/L, desodiation at ~0.7V) [24] and Na_3Sb (660 mAh/g, 1120 Ah/L, desodiation at ~0.8V)[25]. It should be noted that these volumetric capacities were calculated at the full volume expanded states, as the electrochemical alloying process of sodium with other elements is usually accompanied by a huge volume expansion which must be accommodated in a battery.[26] Tin phosphide (Sn_4P_3) was found to be an interesting material as anode electrode for sodium ion batteries with a high volumetric capacity.[27,28] The reaction mechanism of Sn_4P_3 will be discussed in Chapter 4.

On the other hand, the significant volume change during charging/discharging can lead to the cracking and pulverization of electrode particles. After successive cycles, electrode particles may lose electrical contact which results in capacity fade. One possible solution is to use an inactive phase to dilute the volume expansion and thus, reduce the volume change. Inactive phases can be introduced to the system by the use of conversion reactions.[29,30] In a conversion reaction, the general reaction can be written as

$$M_aX_b + (bc)Na \rightleftarrows aM + bNa_cX \qquad\qquad (1.1)$$
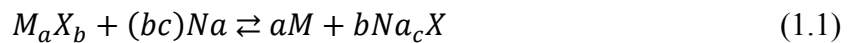
Where M is the inactive phase toward sodiation and X is the electrochemical active phase that can react with sodium. Conversion reactions that involve transition metal phosphides will be discussed in Chapter 5.

CHAPTER 2   BACKGROUND

In this chapter, the fundamentals of lithium-ion batteries will be described, followed by a description of the current state of the research in sodium-ion batteries. Lithium-ion batteries and sodium-ion batteries share similar chemistries, and the operating mechanism of sodium ion batteries can be seen as an analogous to lithium-ion batteries. Therefore, an introduction to lithium-ion batteries, which is already a relatively mature technology, is given here as a basis for understanding sodium-ion battery chemistry.

2.1   LITHIUM –ION BATTERIES

Lithium-ion batteries are comprised of three main components: a negative electrode (anode), a positive electrode (cathode) and an electrolyte. The negative and positive electrodes are attached to current collectors, which is usually copper foil for the negative electrode and aluminum foil for the positive electrode. Both negative and positive electrodes are composite materials, prepared from active material powders, binders and conductive additives. The active materials are usually in the form of layered compounds that can host lithium ions in the interlayers, or spinel materials that contain tunnels. A porous membrane separator containing electrolyte is used to separate the negative electrode from the positive electrode. The separator is usually made from electrically insulating polymers, so as to keep the positive and negative electrodes electrically isolated. When the cell is being charged or discharged, an external circuit connects the positive electrode and the negative electrode, allowing current flow through. A schematic diagram of a lithium-ion battery is shown in Figure 2.1.
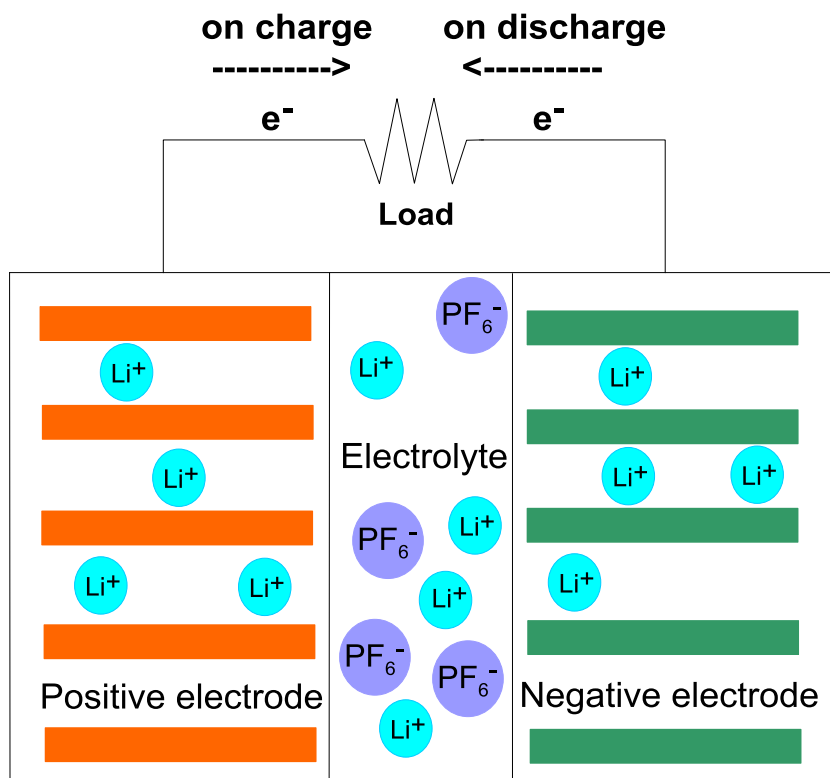
Figure 2.1 Schematic of a lithium-ion battery. The positive and negative electrodes are layered lithium transition metal oxide ($LiMO_2$) and graphite, respectively. The electrolyte salt is $LiPF_6$.

During the charge of a lithium-ion battery, the negative electrode acts as a cathode and positive electrode acts as an anode. An external voltage is applied during charge, which causes the positive electrode to have a higher chemical potential than the negative electrode. Lithium ions can be removed from the positive electrode, to the negative electrode through electrolyte. At the same time, electrons are removed from the positive electrode to the negative electrode through the external circuit. After fully charging, lithium vacancies exist in the positive electrode, while the negative electrode is lithium-rich.

The discharge process is driven by the difference between the chemical potential of positive electrode and negative electrode. In this case, the negative electrode acts as anode and the

positive electrode acts as cathode. As the positive electrode has a lower chemical potential than the negative electrode, lithium ions spontaneously travel from negative electrode to the positive electrode through electrolyte when an external circuit is connected to the battery. The electrons simultaneously travel from the negative electrode to the positive electrode via the external circuit. After fully discharging, there should be no little or no lithium in the negative electrode. The working voltage of such a cell can be expressed as

$$E = -\frac{(\mu_{cathode} - \mu_{anode})}{e} \qquad (2.1)$$

where $\mu_{cathode}$ and μ_{anode} are the chemical potentials in electron volts (eV) of the cathode and the anode, respectively, and e is the charge of an electron.

2.1.1   Positive electrode materials

The positive electrode material of a lithium ion battery is often a lithium transition metal oxide or polyanion-based lithium compound. There are many types of commercial lithium transition metal oxides, including layered lithium transition metal oxides and spinel lithium transition metal oxide. $LiCoO_2$ (LCO) is a typical layered lithium transition metal oxide and has been the most widely used positive electrode material since the first introduction of commercial lithium ion batteries.[31] However, cobalt is scarce and expensive, as stated above. Due to its high cost and to improve thermal stability, researchers have been studying the substitution of cobalt with other metal, such as nickel, manganese, aluminum, etc. Of all the studies, two types of materials have shown particularly successful in regards to performance and economics, NMC (Lithium Nickel Manganese Cobalt Oxide)[32,33] and NCA (Lithium Nickel Cobalt Aluminum Oxide)[34]. NMC and

NCA are now being used in about 1/3 of the cathode materials. Presumably, they will keep expanding their market share in the future.[7] Spinel lithium transition metal oxide has a general formula of LiM_2O_4, where M is usually Mn, as in $LiMn_2O_4$. These types of materials offer high rate capability due to the 3D networks of crystal structure. Mn is also inexpensive and environmentally friendly.[35,36] Doping with Mn and Ni, such as in $LiNi_{0.5}Mn_{1.5}O_4$, results in high operating voltages (~4.7 V versus Li^+/Li).[37] $LiFePO_4$ (LFP) is the most studied polyanion-based positive electrode. Iron-based compounds are naturally abundant and less toxic than Co, Mn and Ni compounds.[38] The main obstacle with LFP in the early days of its development was the poor ionic and electronic conductivity of LFP. The 1-D tunnels in which lithium-ions diffuse in LFP can be easily blocked by defects and impurities, which limited the rate capability of LFP. By reducing particle size[39] and coating with carbon[40], LFP achieved high-rate capability. However, low operating voltage and the gravimetric and volumetric energy density limit the application of LFP.

2.1.2   Negative electrode materials

A variety of negative electrode materials have been studied in lithium ion batteries. Lithium metal was first used as negative electrode material for commercial rechargeable batteries in the 1980's. Lithium metal has very high volumetric and gravimetric capacity. Because of the low redox potential of lithium (E = -3.04 V versus standard hydrogen electrode), it also gives the battery a high operating voltage and thus a high energy density. However, there are some problems that prevent the use of lithium metal as negative electrode in today's batteries. During the repetitive striping and plating that occurs during cell charge and dischareg, dendrites form on

the surface of lithium metal, which results in high surface area. This leads to poor coulombic efficiency and potential thermal instability from exothermic reactions between lithium metal and electrolyte. In addition, the dendrite may penetrate the separator and cause short circuit of the cell. Therefore, even though there are batteries that employ lithium metal as negative electrode on market,[41] most of the commercial rechargeable batteries today do not use lithium metal as negative electrode.

The use of graphite as negative electrode can avoid dendrite formation. [41]Graphite is the most commonly used negative electrode in Li-ion batteries today. Lithium ions can electrochemically intercalate/deintercalate into the layered structure of graphite. Up to one lithium ion can be inserted for each 6 carbon atoms, forming LiC_6 with a theoretical capacity of 372mAh/g.[42] Graphite is inexpensive and easily accessible. The working potential is low (~0.1 V versus Li^+/Li), providing good energy density. Other advantages of graphite include low voltage hysteresis, good cycling performance, low volume change during charge/discharge, good rate capability and high coulombic efficiency, etc. Extensive research has also been conducted on using alloy materials as negative materials for lithium-ion batteries, such as Li-Si,[43] Li-Sn,[44] etc, as these materials offer higher energy density than graphite. However, the commercialization of alloy materials remains rare, compared to graphite.

2.1.3   Electrolyte

The electrolyte acts as a medium to transport lithium ions back and forth between the positive electrode and the negative electrode in a cell. Electrolyte used in commercial lithium-ion batteries commonly consist of organic solvent and salt. The solvent should possess wide

operating temperature, low viscosity, good electrochemical stability and good salt solubility. The electrolyte should also be able to form a stable solid electrolyte interphase (SEI) on the surface of the electrodes, which will be discussed later. However, often a solvent may satisfy some of these requirements, while lacking in others. Therefore, two or more solvents are then used to have the best performance.[45] $LiPF_6$ is a commonly used salt in commercial lithium-ion batteries because of its solubility and chemical stability. The disadvantage of $LiPF_6$ is its thermal instability and its moisture sensitivity.[46] Other electrolyte systems studied also include ionic liquids and solid/polymer electrolytes.

Electrolytes decompose on solid surfaces at low voltage, and a new surface layer is formed from the decomposition product. This surface layer is called the solid electrolyte interphase (SEI). The composition of the SEI is complicated, consisting of LiF, Li_2O, Li_2CO_3, and others.[47] The SEI is characterized by low electronic conductivity and high ionic conductivity. Therefore it essentially acts as a passivation layer and prevents the electrolyte from further decomposition, while allowing the passage of lithium ions, so the battery can operate normally.[48] Almost all of the electrolyte in today's commercial lithium-ion batteries contain ethylene carbonate (EC). One of the merits of EC is that it forms a good stable SEI on the negative electrodes.[41]

2.2   SODIUM-ION BATTERIES

Sodium-ion batteries are promising as an alternative to lithium-ion batteries. The operating concept of sodium-ion batteries is analogous to lithium-ion batteries. A sodium-ion battery consists of a positive electrode, a negative electrode, and an electrolyte. Sodium ions act as charge carriers and can be shuttled between positive and negative electrodes. Sodium ions can be

guests in both positive and negative electrodes. This shuttling behavior is also called the

"rocking chair model", as sodium ions rock back and forth between two electrodes. Research on

sodium-ion batteries paralleled that of lithium-ion batteries in 1980's.[49–52]However, after the

successful commercialization of lithium-ion batteries, there was a hiatus in the progress of

sodium-ion batteries. During the last few years, the increasing demand for energy storage

systems, while using inexpensive and environmentally friendly materials has led to a renewed

interest in rechargeable sodium-ion batteries.

2.2.1   Positive electrode materials

Like lithium-ion batteries, the most studied positive electrode materials for sodium-ion batteries

are layered transition metal oxides (Na_xMO_2),[53] because of their easy synthesis, high redox

potentials and high energy densities. There are two main groups of layered sodium transition

metal oxides: P2 and O3, according to Delmas' notation, where P and O refer to the local

environment around the sodium atoms as either prismatic or octahedral, respectively, and the 2

and 3 indicate the repeat period of transition metal layers. [54] The P2 phase generally has about

1/3 sodium deficiency in the composition. While both P2 and O3 phases are electrochemically

active towards reversible sodiation/desodiation, the P2 phase usually delivers a better overall

electrochemical performance than O3.[53] The structure and electrochemistry of layered sodium

transition metal oxides $NaMO_2$ (M= Cr, Mn, Fe, Co, Ni, Cu) have been studied since the

1980's.[55–63] $NaVO_2$ and $NaTiO_2$ were not included in the series because their operating voltages

are relatively low and are usually considered as negative electrodes.[64–67]Due to the larger radius

of the sodium ion compared to the lithium ion, a stronger structural reordering or phase transition

12

during sodiation/desodiation is often observed, resulting in a stepwise voltage curve and, often, poor cyclability.[10]

Binary, ternary and beyond $NaMO_2$ systems have been studied in order to solve the problems of poor capacity retention and structural instability. Some show promising performance comparable to that of lithium-ion battery cathodes. Komaba et al. synthesized and characterized P2-$Na_{2/3}Mn_{1/2}Fe_{1/2}O_2$, made of earth-abundant elements, which delivers an energy density of 520 Wh/kg or 2132 Wh/L.[12] In comparison, LFP, LCO and NMC deliver energy densities of 1980 Wh/L (charged to 3.8 V), 2950 Wh/L (charged to 4.2 V) and 2870 Wh/L (charged to 4.3 V), respectively. Substitution of electrochemically inactive metals, such as Mg or Al, in the transition metal layer also enhances the capacity retention.[68] Bruce et al. investigated P2-$Na_{0.67}Mn_{1-y}Mg_yO_2$ (y=0, 0.05, 0.1, 0.2). They showed that the substitution of Mn by Mg can improve capacity retention and decrease voltage polarization.[69]

Other materials investigated as sodium-ion batteries positive electrode include polyanionic compounds and Prussian-blue analogues. Polyanionic compounds with open structures offer another possibility as positive electrode for sodium ion batteries. A series of polyanionic compounds based on phosphates,[70] sulfates,[71] fluorophosphates[72] have been studied. NASICON compounds $Na_3V_2(PO_4)_3$ shows a capacity of 120 mAh/g at a voltage of 3.3V, resulting in an energy density of 400 Wh/kg.[73] The drawbacks of polyanionic compounds include low capacity and energy density.

It should be noted that most layered sodium transition metal oxide materials suffer from air-sensitivity. Rigorous protection of the materials against ambient atmosphere is needed to obtain good electrochemical performance. Nazar et al. revealed that the exposure of $Na_xMn_{0.5}Fe_{0.5}O_2$ to

moisture or CO_2 will result in higher hysteresis and lower capacity.[74] Therefore, in order for sodium ion batteries to have practical application, more studies on positive electrode materials with improved air stability are required.

2.2.2   Negative electrode materials

CARBON-BASED MATERIALS

In contrast to the optimistic progress in positive electrode materials, the development of negative electrode materials for sodium-ion batteries remain a tough challenge. Graphite is widely used as the negative electrode in lithium-ion batteries, which forms a stoichiometry of LiC_6 at full lithiation. However, Na^+ cannot insert into graphite to any appreciable degree at ambient pressure. The interlacation of sodium into carbon can be achieved using a hard carbon with disordered graphene sheets, as discovered by Stevens et al.[19] Researchers have associated the electrochemical performance of hard carbon with a "house of cards" model.[75–77]Figure 2.2 shows a "house of cards" model of hard carbon for sodium intercalation.[78] Sodium can be either inserted between the nearly parallel graphene sheets or be absorbed into the pores formed by graphene sheets. Stevens et al. found that sodium ions can reversibly intercalate into hard carbon and form Na_xC_6, with a reversible capacity of about 300 mAh/g at low voltage.[19] This is comparable to the capacity of graphite in lithium-ion batteries (372 mAh/g). However, much of the capacity occurs below 50 mV, which cannot be utilized in a practical cell. In addition, the density of hard carbon is low (1.5 g/cm^3) compared with graphite (2.1 g/cm^3), leading to a lower volumetric capacity of 450 Ah/L, compared with 750 Ah/L of graphite in lithium-ion batteries. For applications such as electric vehicles, volumetric capacity is often more important than

gravimetric capacity. Therefore, a better negative electrode with performance comparable to that

of lithium-ion batteries is needed for the commercialization of sodium-ion batteries.

Sodium ions in the nanopores betweenrandomly stacked layers

Sodium ion between graphene sheets
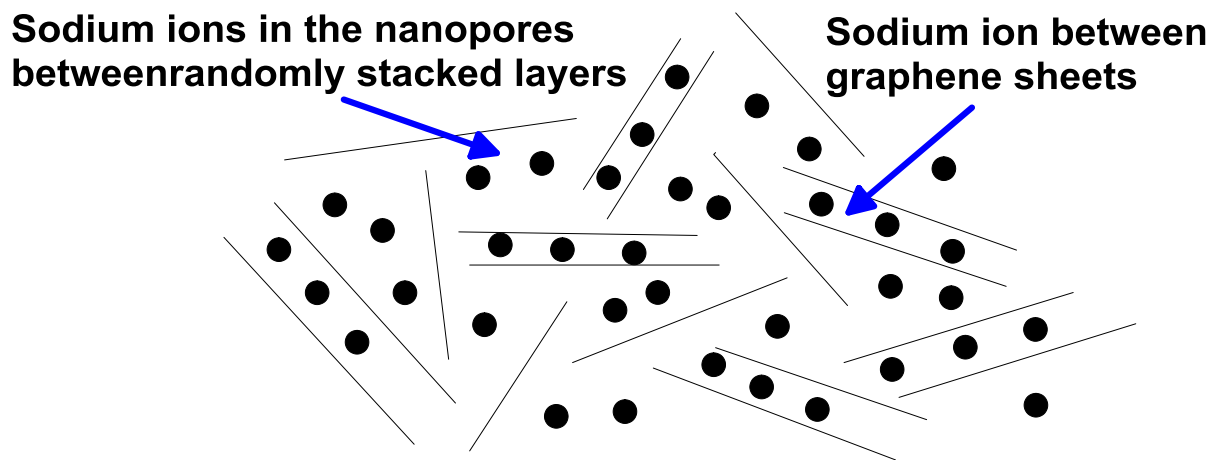
Figure 2.2 "House of cards" model of hard carbon and intercalated sodium ions

ALLOYS

Alloys have long been considered and studied as candidates for negative electrode materials of

lithium/sodium-ion batteries. Many Group 14 and 15 elements (Si, Ge, Sn, Pb, As, Sb, Bi) are

known to form binary alloys with sodium. Chevrier et al.[79] calculated the voltage of Na-Si, Na-

Ge, Na-Sn and Na-Pb alloys using DFT (density functional theory). Their study shows that alloy

negative electrodes generally have low operating potentials (usually below 0.5V versus Na+/Na)

and therefore are suitable for negative electrodes. They also suggested that the volumetric energy

density of Na alloys is lower than that of Li alloys. In 2012, Ellis et al. [21] showed the sodiation of

tin with a reversible capacity close to the theoretical value (847 mAh/g) and the formation of

$Na_{15}Sn_4$ at full sodiation. Monconduit et al. [25] showed the reversible sodiation of bulk antimony

with good cycling performance. Reversible sodiation of lead and bismuth has also been

reported.[24] Compared to intercalation materials, alloy materials can react with a larger number of

sodium ions and deliver much higher capacity. There are generally three types of alloys formed at the most Na-rich state, as NaX, $Na_{15}X_4$ and Na_3X, The three types of sodium alloys are shown in Figure 2.3 with their corresponding theoretical specific capacities and volumetric capacities. It should be noted that while Si readily reacts with Li in an electrochemical cell, the reversible sodiation of Si have not yet been observed experimentally in an electrochemical cell, even though the NaSi phase does exist.
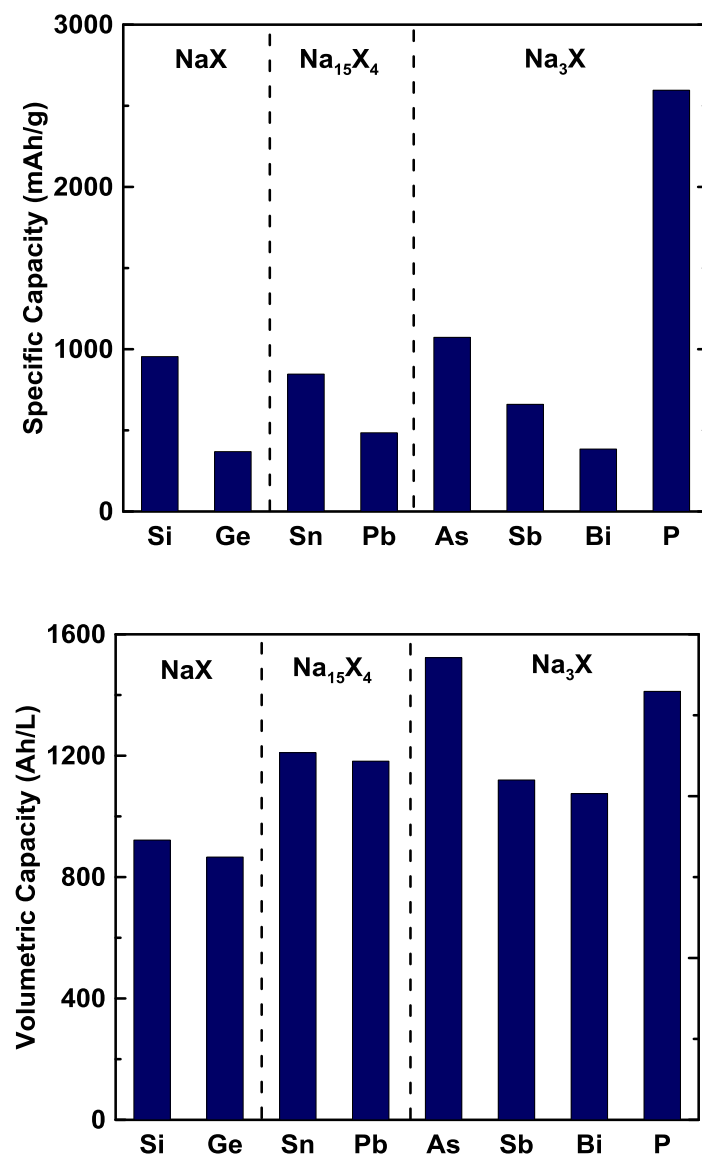
Figure 2.3 theoretical specific capacities and volumetric capacities of alloy materials

16

A problem with using alloy negative materials is their huge volume expansion during sodiation, which results in electrode fracturing and poor long-term cycling performance. Common strategies include optimizing binders, electrode structures, and electrolyte additives. Advanced binders such as carboxymethyl cellulose (CMC) [80] and polyacrylic acid (PAA)[81] were shown to provide better cycling performance over poly(vinylidene fluoride) (PVDF) binder. Komaba et al. [82] showed that using fluorinated ethylene carbonate (FEC) additive in electrolyte can significantly improve the cycle performance, owing to the formation of stable SEI by the decomposition of FEC. Qian et al. [83] reported the preparation of Sb/C composite electrode from mechanical ball-milling, which delivers a capacity of 600 mAh/g and 94% capacity retention over 100 cycles.

PHOSPHORUS AND PHOSPHORUS-BASED MATERIALS

Phosphorus is a non-metallic element of Group 15. There are seven known binary Na-P phases: Na_3P, NaP, Na_3P_7, Na_3P_{11}, NaP_5, NaP_7 and NaP_{15}. [84] Phosphorus has a very high theoretical capacity (~2596 mAh/g or 1412 Ah/L), assuming the fully sodiated product is Na_3P. This capacity is several times higher than those of sodium alloys. Previously, researchers have studied the use of phosphorus-based materials as the negative electrode for lithium-ion batteries and showed some interesting results.[85,86]Phosphorus can reversibly accommodate 3 lithium ions and form Li_3P. However, the operating voltage is somewhat high (lithiation at ~0.8V, delithiation at ~1.1V) for a negative electrode, which will result in a low energy density full cell. Because the higher electrochemical standard potential of Na^+/Na compared to that of Li^+/Li, one can expect that the operating voltage may be suitable for sodium-ion battery negative electrodes. In 2013,

Qian el al. [23] and Kim et al. [22] simultaneously showed the use of phosphorus/carbon composite as a negative electrode material in sodium cells with high capacity (~1800 mAh/g) and good cyclability. The sodiation voltage is ~0.2V while the desodiation voltage is ~0.6V, appropriate for negative electrode. Recently, Komaba et al. reported a detailed study on the phosphorus electrodes in sodium-ion batteries.[87] They found that the sodiation product, Na_3P is highly reactive and causes electrolyte decomposition. By using FEC additive, electrolyte decomposition can be effectively suppressed and the cycle performance improved. They also reported that by lowering the charge voltage from 2.0 V to 0.8 V, the cyclability is further improved while not much capacity is compromised. This is because the phosphorus-containing SEI is oxidized at voltages above 0.8 V.

Phosphorus containing compounds such as metal phosphides have also been reported in sodium-ion batteries. Fullenwarth et al.[30] showed that NiP_3 undergoes a conversion reaction upon sodiation and delivers a reversible capacity of ~900 mAh/g over 20 cycles. The voltage curve is similar to that of elemental phosphorus and a reversible conversion reaction is observed. Qian et al.[27] and Kim et al.[28] reported that Sn_4P_3 showed good performance in sodium-ion batteries. Sn_4P_3 offers a reversible capacity of ~700 mAh/g at low voltage. $Na_{15}Sn_4$ and Na_3P were observed after full sodiation. Moreover, the volume expansion of Sn_4P_3(93%) is much smaller than that of a P/C composite (187%).[28]

It should be noted that there are some disadvantages regarding phosphorus as negative electrodes. The poor electronic conductivity of phosphorus requires a large amount of conductive material, such as carbon black to increase the conductivity, which would lower the energy density. [28]The large volume expansion of phosphorus during sodiation usually leads to poor cyclability. The large voltage hysteresis lowers the charge/discharge energy efficiency. In

addition, the sodiation product of phosphorus (or phosphide), Na_3P, readily reacts with the water

in air and form toxic phosphine (PH_3), which can limit their practical use. Therefore, there is still

a long way to go before phosphorus-based materials to have any practical application, if ever.

CHAPTER 3   EXPERIMENTAL METHODS

In this section, some basic concepts of X-ray Diffraction (XRD) and Mössbauer spectroscopy

will be illustrated, followed by the description of the process for electrochemical testing.

3.1   X-RAY DIFFRACTION

X-ray diffraction (XRD) is a commonly used technique to identify the structure of a sample. X-

rays were discovered by Wilhelm Conrad Röntgen in 1895. X-ray has a wavelength range of

0.01 to 10 nanometers, which is on the same scale of the distance between lattice planes in a

crystal. In 1912, Max von Laue discovered the diffraction of X-rays by crystals. One year later,

William Henry Bragg and his son William Lawrence Bragg developed Bragg's law, which

connects the observed diffraction with the lattice planes of crystal structure.

The most common source of X-rays used for XRD is a copper X-ray tube (other metals such as

molybdenum or tungsten are typical as well). For a copper X-ray tube, the tube is in vacuum and

contains a tungsten filament cathode and a copper anode, with a voltage difference (~45 kV)

between the cathode and anode. The cathode is heated to produce electrons and the electrons are

accelerated toward the anode by the voltage difference. The inner shell electrons of the copper

anode can be knocked out by the accelerated electrons and electrons in the outer shell drop to

lower energy levels immediately to fill the vacancy, emitting characteristic X-rays with energies

equal to the energy difference between orbitals.

Cu-K_α X-ray radiation was used here for XRD. A K_α emission occurs when an electron

transitions from the 2p orbital of the L shell to K shell. Due to the spin-orbit interaction, two

orbitals exist within the 2p orbital, $2p_{1/2}$ and $2p_{3/2}$. Therefore, K_α radiation actually consists of

$K_{\alpha1}$ and $K_{\alpha2}$ radiation, corresponding to the energy difference between the $2p_{1/2}$ and the K shell, or the $2p_{3/2}$ and the K shell. Because $2p_{3/2}$ has a slightly higher energy level than $2p_{1/2}$, $K_{\alpha1}$ radiation has a higher energy and a shorter wavelength than $K\alpha_2$ radiation. The wavelength of both $K_{\alpha1}$ radiation and $K_{\alpha2}$ radiation is approximately 1.54 Å. The $K_{\alpha1}$ and $K_{\alpha2}$ lines have the strongest intensity among all the X-rays emitted from the copper X-ray tube, therefore they are used for the XRD of crystals. Other low intensity x-radiation, such as K_β radiation, can be removed by a filter or monochromator.
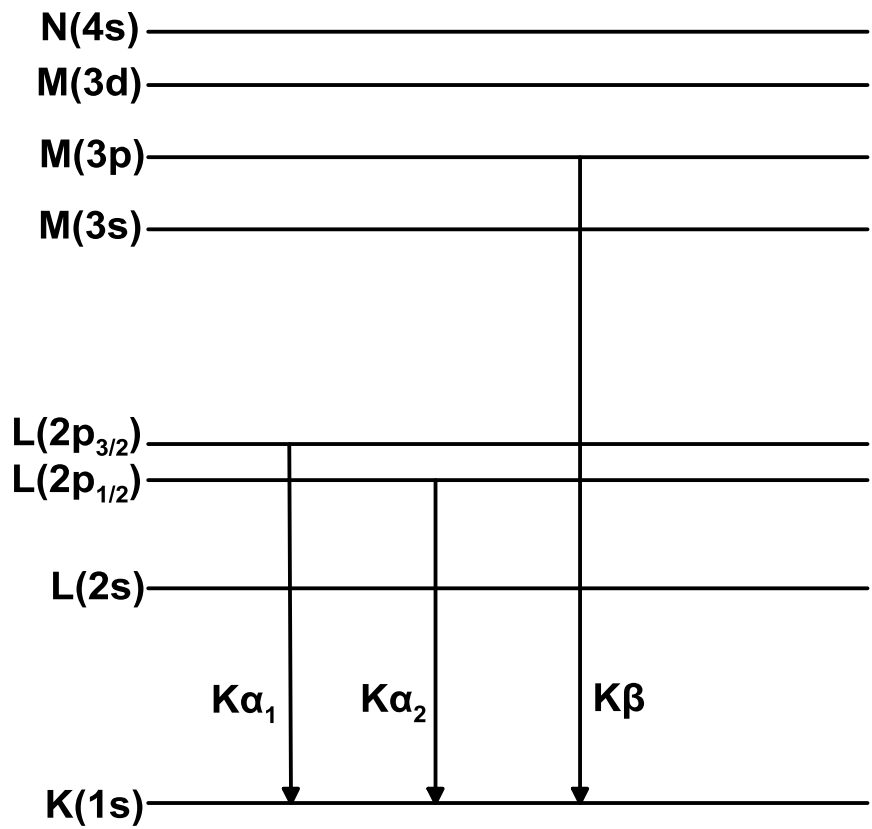
Figure 3.1 Generation of copper Kα and Kβ X-rays

Once X-rays leave the X-ray tube, a series of slits and monochromators are typically arranged along the path of the X-ray beam, to control the wavelength and width of the incident beam

needed for the diffraction. The X-rays then strike the sample and because the wavelength of X-rays and the interatomic distances are on the same order of magnitude, X-rays can be diffracted. The diffracted X-rays have the same wavelength as the incoming X-ray.
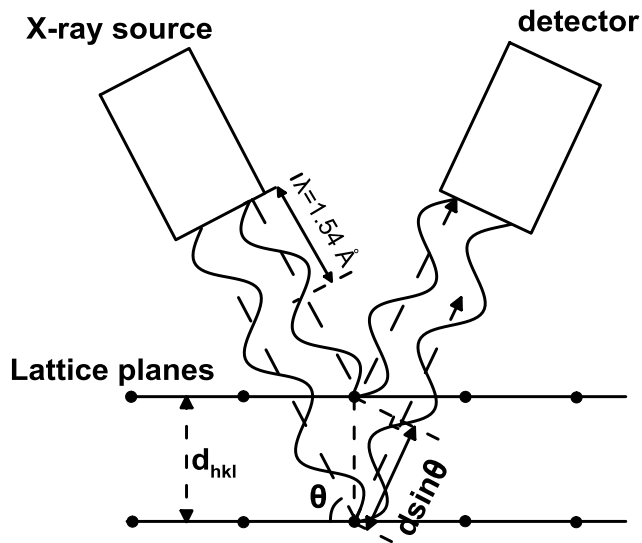
Figure 3.2 Bragg scattering from lattice planes in a crystal structure

As shown in Figure 3.2, the diffracted X-rays have the same angle as the incident X-rays. The intensity of diffracted X-rays is continuously recorded as the X-ray source and detector rotate through the same angle. The obtained XRD data is plotted as intensity versus the scattering angle, 2θ. For a fixed X-ray wavelength, constructive interference and a peak in intensity occur when the distance between two lattice planes and the angle θ satisfy the Braggs' Law:

$$2\,d\,\sin\theta = n\,\lambda \qquad\qquad (3.1)$$

Where d is the distance between lattice planes, θ is the angle of the incident X-rays to the sample, n is an integer, λ is the wavelength of the X-rays used (~1.54 Å). $2d\sin\theta$ is the path length difference between X-rays scattered from adjacent lattice planes. When the diffracted beam is retarded by an integral number of wavelengths, constructive interference occurs and the peak intensity increases. When the diffracted beam is retarded by an odd multiple of half the wavelength, destructive interference occurs and there is no peak.

Miller indices are used to define the crystal lattice planes. For a given set of lattice planes, three lattice vectors, a_1, a_2, and a_3, define a unit cell. The reciprocal of the intercepts of the lattice planes along the lattice vectors, h,k and l, are defined as Miller indices. h, k and l are written in integers with their greatest common divisor as 1. For a simple crystal, such as a cubic crystal, the spacing, d, between adjacent (hkl) lattice planes is

$$d = \frac{a}{\sqrt{h^2+k^2+l^2}} \qquad (3.2)$$

where a is the lattice constant of the unit cell, h, k and l are the Miller indices of the specific lattice plane. Other crystal families have different formulas that relate h, k and l with the spacing d. The distance between adjacent lattice planes can be calculated using Braggs' Law, and the peaks can be associated with their specific lattice planes. Further detailed characterization can be done using Rietveld refinement by fitting XRD intensities calculated from trial atom positions to the experimental data. Rietveld refinement can be performed by computer program such as Rietica.[88] The experimental data can also be compared with a database for phase identification by using computer program such as Match!(Crystal Impact).[89]

3.1.1 XRD Measurements

XRD measurements were made with a Rigaku Ultima IV powder diffractometer equipped with a Cu Kα X-radiation source and a scintillation detector with a diffracted beam monochromator. A filament current of 40 mA and an accelerating voltage of 45 kV were typically used to generate X-rays. For non-air sensitive samples, sample powders were poured into a stainless steel sample well with a dimension of 25 mm × 20 mm × 3 mm on a stainless steel plate. The sample was then pressed down and packed with a glass slide to create a flat upper surface that was coplanar with the top of the sample holder before measurement. For air-sensitive samples, as shown in Figure 3.3, a specially designed air-sensitive sample holder was used. The sample holder has an arc-shaped aluminized Mylar window so that it is perpendicular to the incident and scattered X-ray beam and does not contribute to the detected X-ray diffraction. Sample preparation of air-sensitive samples was conducted in an Ar-filled glovebox. XRD measurements for both air-stable and air-sensitive samples were collected at a typical scattering angle range of 10 to 80 degrees 2-theta with a step of 0.05 degrees between each measurement.

Figure 3.3 Air sensitive XRD holer before (left) and after (after) assembly

3.2 CHRACTERIZATION USING MÖSSBAUER SPECTROSCOPY

The Mössbauer effect was first discovered by Rudolf Mössbauer in 1957. This effect employs recoil-free resonant absorption and emission of gamma rays in solid to study the energy levels of nuclei in atoms, which are influenced by their surrounding environment. Room temperature Mössbauer spectroscopy is most commonly used to study iron based alloys, although tin based samples are also frequently studied. The Mössbauer effect is a useful tool for probing amorphous materials, since very little information can be extracted using conventional XRD techniques.

3.2.1   Recoil-free fraction

Atomic nuclei can undergo a variety of energy level transitions, associated with the emission or absorption of a gamma ray. During emission or absorption of a gamma ray, a free nucleus recoils due to conservation of momentum, with a recoil energy, E_R. Therefore the emitted gamma ray has E_R less energy than the transition energy. However, due to the recoil of absorbing nucleus, in order for the gamma ray to be absorbed by the nucleus, the gamma ray must have E_R more energy than the transition energy. On the other hand, due to thermal motion, the nucleus would be constantly moving, which causes a Doppler effect energy, E_D. This produces a profile as shown in Figure 3.4.
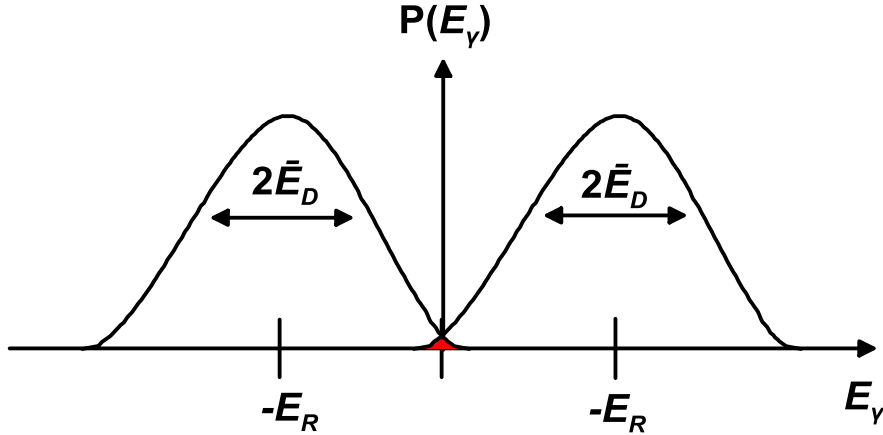
Figure 3.4 Resonant overlap in free atoms. Adapted from Reference [90]

For a resonant absorption to occur, the energies of emission and absorption must overlap and this is shown in the red-coloured region. The red-coloured region is exaggerated in Figure 3.4, as in reality it is extremely small, making the use of resonant absorption/emission an impractical technique.

However, if the nuclei of both emitter and absorbed are within a solid matrix, the effective recoiling mass is now the mass of the whole system, which is much larger than the mass of a single nucleus. Also because of the chemical binding in the crystal lattice, the recoil of the single nucleus is too small to be transmitted to the whole system, making the recoil energy of the whole system almost zero. In this situation, E_R and E_D both approach zero. Therefore the emission and absorption peaks shift towards each other (towards the incident energy) and become narrower, which make the overlap area increases. This is called the Mössbauer effect. The probability of the overlap between absorption and emission peaks is called the recoil-free fraction, f, and is given as

$$f = 1 - \frac{E_R}{\hbar\omega} \qquad (3.3)$$

where $\hbar$ is the reduced Planck constant and ω is the photon angular frequency.

3.2.2   Center shift

As the environment of the nuclei we want to study would usually be different from the source, the energy of the emission gamma-rays should be variable so it could match the absorption energy. This energy variation can be achieved by the use of the Doppler effect. In a Mössbauer experiment, the gamma-ray source is oscillated towards and away from the absorber so it produces a series of gamma-rays with different energies. The velocity of the oscillating gamma-ray source relative to the absorber is then recorded. Typically, Mössbauer Spectroscopy is plotted as the transmission counts vs. the relative velocity (in mm/s).When the emitted gamma-ray energy matches the energy of a nuclear transition in the absorber, the gamma-rays are resonantly absorbed and we see a peak in the Mössbauer spectrum, as shown in Figure 3.5.
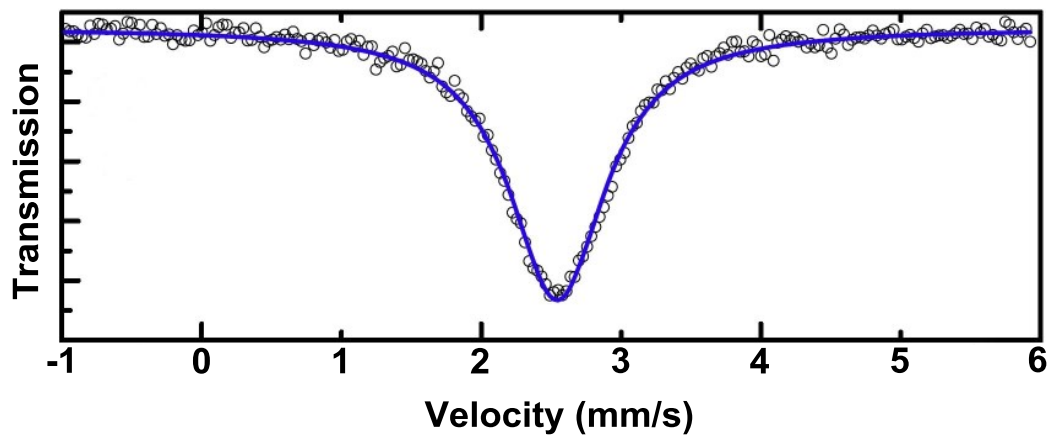

Figure 3.5 Mössbauer spectrum of pure Sn, showing the velocity scale and transmission counts, as adapted from Reference [91]

In Figure 3.5, the absorption peak occurs at around 2.54 mm/s, indicating that the source and absorber are not the same. Any difference in the s-electron environment between the source and absorber produces a non-zero resonant peak shift. As the shift cannot be measured directly, it is usually quoted relative to a known absorber. For example, ^{119}Sn Mössbauer spectra will often be quoted relative to BaSnO$_3$ (center shift defined as 0 mm/s) at room temperature. The position of the peak relative to the position of BaSnO$_3$ is called its center shift. Positive or negative shifts of the peak are due to the changes in both the localized 5s and 5p electron concentration on the Sn atoms, where the 5s electron concentration is the most significant factor, as described in reference [92,93]. It has been shown that for Sn,

$$CS = -0.45 + 3.1N_s - 0.2N_s{}^2 - 0.17N_pN_s \qquad (3.4)$$

where CS is the center shift, N_s and N_p are the number of effective 5s electrons and 5p electrons, respectively.

3.2.3   Quadrupole splitting

Nuclei with a spin quantum number greater than 1/2 have a non-spherical charge distribution. The non-spherical charge distribution produces an asymmetrical electric field and a quadrupole moment. The quadrupole moment can interact with the electric field gradient and splits the nuclear energy level. The splitting is called quadrupole splitting, which produces two lines of equal intensity in the Mössbauer spectrum. The center of the quadrupole splitting is the center shift. The separation between the quadrupole splitting can be used to measure the asymmetricity of the chemical environment of the nuclei.

As shown in Figure 3.6, for an isotope with a I=3/2 state, such as [119]Sn, there are two excited

states: $I_z = \pm 3/2$ and $I_z = \pm 1/2$. This gives a two line spectrum or a 'doublet' in the Mössbauer

spectrum.
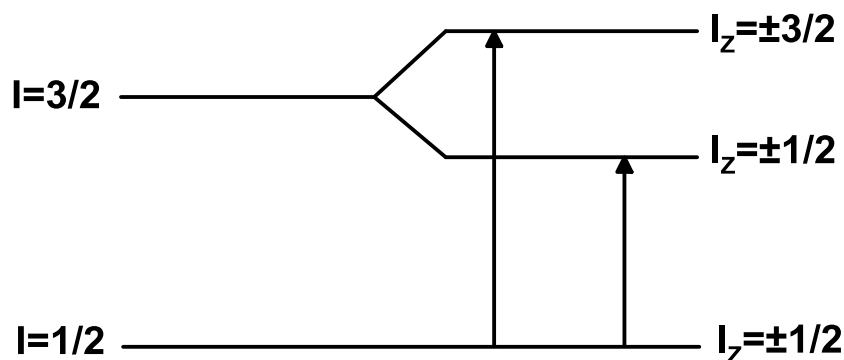
Figure 3.6 Quadrupole splitting for a 3/2 to 1/2 transition.

MÖSSBAUER SPECTROSCOPY MEASUREMENT

For ex-situ electrode samples, several cells were opened at the same cut-off voltage in order to

gain sufficient mass for Mössbauer spectra. Electrodes were removed from the cell and stacked

together into a circular plastic Mössbauer holder. For powder samples, the same kind of

Mössbauer holder was used to hold the powders. The holders were heat sealed in metallized

plastic pouches in an Ar-filled glovebox. Room temperature [119]Sn Mössbauer spectra were

recorded in a constant-acceleration Wissel System II spectrometer equipped with a $CaSnO_3$

source. The spectrometer was calibrated using a composite absorber made of $BaSnO_3$ (room

temperature center shift 0 mm/s) and metallic Sn (room temperature center shift +2.56 mm/s).

All Mössbauer spectra were analyzed with the Recoil software package. [94]
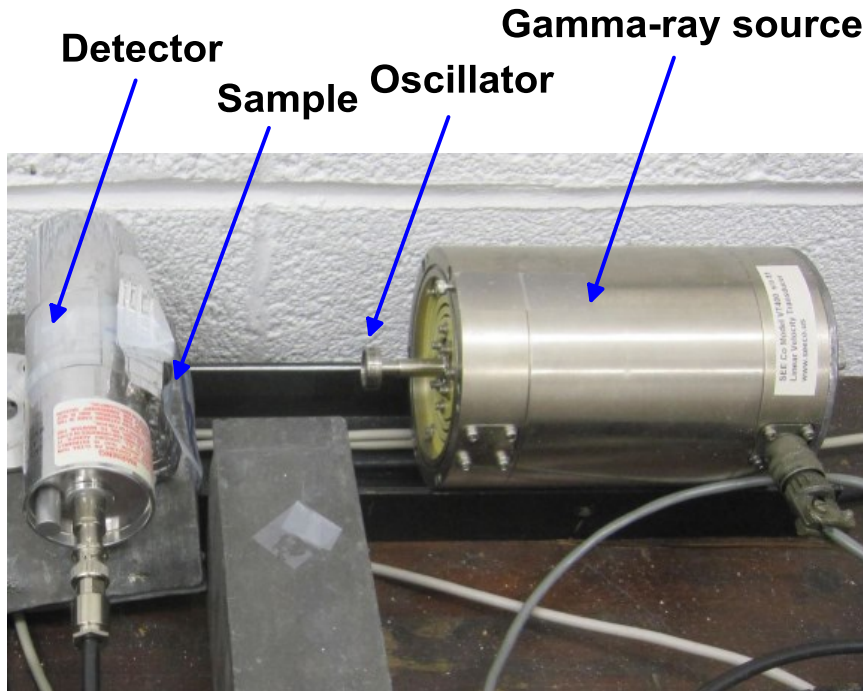
Figure 3.7 Mössbauer sample holder and Mössbauer spectroscopy measurement

3.3   ELECTROCHEMICAL METHODS

3.3.1   Cell Fabrication

In this thesis, composite electrodes made from sample powders were fabricated for all the electrochemical measurements. Typically, composite electrodes consist of an active material, a binder and a conductive additive on a current collector. The binder used was either poly(vinylidene fluoride) (PVDF, HSV 900, KYNAR) or polyimide (PI-2555, HD Microsystems, 20% in N-methyl-2-pyrrolidone). The conductive additive used was carbon black (Super P, Erachem Europe). Active material, binder and conductive additive in a typical weight

ratio of 8:1:1 were mixed in an appropriate amount of N-methyl-2-pyrrolidone (Sigma Aldrich, anhydrous 99.5%) with two tungsten carbide balls in a Retsch PM200 rotary mill (100 rpm, 1 hour) to create a uniform slurry. The slurry was then spread onto aluminum foil with a coating bar having a 0.004 in. gap (cells for Mössbauer studies were made using a coating bar with a 0.012 in. gap) and dried under vacuum at 120 °C overnight. 1.3 cm^2 circular electrodes were punched from the resulting coatings. The electrodes made with PI binder were heated at 300 °C for 3 hours in flowing Ar before being taken into a glove box.

Half-cells were made for electrochemical studies. Electrodes were assembled in 2325-type coin cells in an Ar-filled glovebox. Na disks punched from thin foil (~0.015 inch) rolled from sodium ingot (Sigma Aldrich, ACS reagent grade) were used as counter/reference electrodes. Two Celgard 2300 and one blown microfiber separator (3M Company) were used as separators. 1 M $NaPF_6$ (Aldrich, 98%) in a solution of ethylene carbonate (EC), diethyl carbonate (DEC) and monofluoroethylene carbonate (FEC) (volume ratio 3:6:1, from BASF) was used as electrolyte. As shown in Figure 3.8, the working electrode was placed on top of the cell can bottom. Then one layer of Celgard, one layer of BMF and another layer of Celgard were added as separators. An appropriate amount of electrolyte was added in each layer. A piece of sodium foil was then placed on this stack (not shown in Figure 3.8). Finally a spacer and a conical spring were added to apply an appropriate pressure on the electrodes followed by the cell can top. The cell was then placed in two sequential crimpers to be properly sealed.
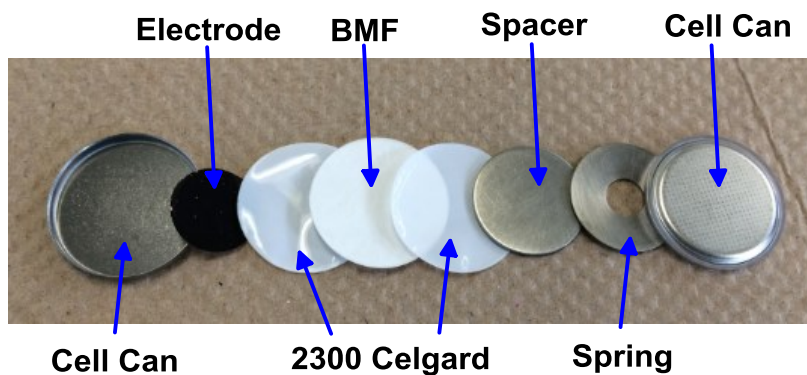
Figure 3.8 Exploded view of a 2325-type coin cell. Note that there should be a sodium
foil (not shown here) between the Celgard and the spacer.

For cells cycled at 60 °C, Conflat cells (as described in Reference [95]) were constructed.
Standard 2.125" (53.18 mm) stainless steel Conflat vacuum fittings were purchased from Nor-
Cal Products, Inc., Yreka, CA USA. Modifications to the fittings were made by DPM Solutions
Inc. of Hebbville, NS Canada. The detailed design and modification of the fittings are described
in reference [95]. Two Celgard 2300 and one blown microfiber separator (BMF, 3M Company)
were used as separators. Two stainless steel spacers and one stainless steel spring were used to
provide an appropriate internal pressure for the cell. A photograph of the components of a
Conflat cell is shown in Figure 3.9.
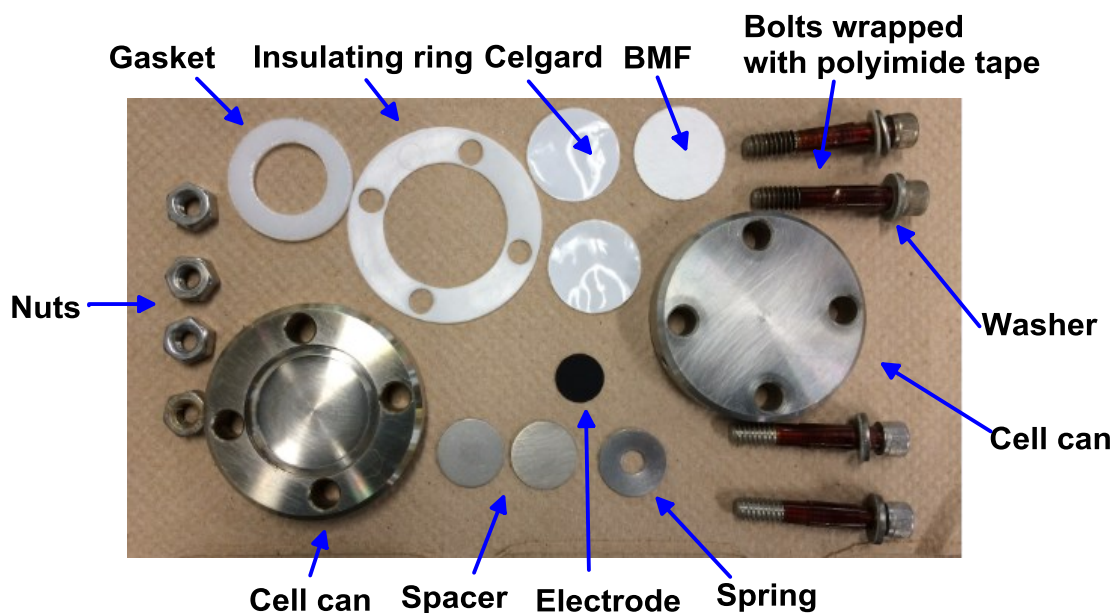
Figure 3.9 Components for a Conflat cell

3.3.2   Electrochemistry

For either Conflat cells or coin cells, electrochemical techniques were used to characterize the electrochemical performance of the electrode materials. All the cells fabricated in this thesis were cycled under thermostatically controlled conditions (± 0.1°C) using a Maccor Series 4000 Automated Test System (Maccor Inc., Tulsa OK). The ambient temperature of cycling cells was either 30.0 °C or 60.0 °C. The electrode materials in this thesis were tested as positive electrode materials in Na half-cells, but would be used as negative electrode materials in full cells.

Most cells were cycled between 0.005 V and 1.5 V at constant current rates. Currents are expressed as "C-rate". The theoretical capacity of a cell (in Ah or mAh) divided by desired charge/discharge time (typically in h) is the cycling current. For example, a C/20 rate means that

the cell would be fully discharged/charged at the constant current in 20 hours to reach its theoretical capacity.

Electrochemical testing resulted in a measurement of cell capacity, coulombic efficiency, and cycle life. Capacity is determined by multiplying the current by the charge/discharge time. The unit of capacity is either mAh or Ah. The gravimetric capacity of an electrode material is usually expressed as mAh/g, which is the measured capacity divided by the active mass of the material. Volumetric capacities are measured in mAh/cm^3 or Ah/L, which is calculated by using the measured capacity and volume at maximum expansion. The coulombic efficiency is defined as the charge capacity divided by the discharge capacity of the previous half-cycle. In this thesis, Maccor Series 4000 Automated Test System was used to measure the coulombic efficiency, which has an accuracy of ~1470 ppm.[96] Cycle life is the long-term cyclability of the electrode material, which is typically the number of charge/discharge cycles before the battery becomes unusable.

CHAPTER 4   ELECTROCHEMICAL REACTION MECHANISM OF TIN

PHOSPHIDE WITH SODIUM

4.1   INTRODUCTION

Sn has high theoretical volumetric capacity and low desodiation voltage.[21] However, the capacity of metallic Sn decreases quickly during charge/discharge cycling; in contrast, Sn-containing compounds can provide better cycle life. Sn_4P_3 is a promising anode material for sodium ion batteries. It has a theoretical capacity of 1132 mAh/g or 1292 Ah/L, assuming the fully sodiated product is $Na_{15}Sn_4$ and Na_3P. Here, to be reflect their performance in full cells, the volumetric capacity is calculated at full volume expansion. Recently, Qian et al. [27] and Kim et al. [28] reported that using Sn_4P_3 as an anode material for sodium ion batteries provides impressive cycle life (>100 cycles) as well as good reversible capacity (>600 mAh/g or 700Ah/L).

This study aims to provide a deeper understanding of the sodiation mechanism of Sn_4P_3 using ex-situ X-ray diffraction (XRD) and Mössbauer spectroscopy. Room temperature [119]Sn Mössbauer spectroscopy has been successfully used to help understand the mechanism of Sn or Sn-containing compounds during the reversible lithiation or sodiation process.[93,97]Pérez-Vicente [98] used [119]Sn Mössbauer spectroscopy to explain the lithiuation process of Sn_4P_3, Baggetto et al. [97] and Du et al. [91] used [119]Sn Mössbauer spectroscopy to determine the sodiation extent of Sn. Knowledge from these studies are important to shed light on the sodiation mechanism of Sn alloys. Here the utility of Mössbauer spectroscopy for the investigation of the sodiation mechanism of Sn-containing compounds as anode materials in Na-ion cells is demonstrated.

4.2 EXPERIMENTAL

Materials synthesis, analysis by XRD and Mössbauer spectroscopy and cell assembly are discussed in detail in Chapter 3. Briefly, stoichiometric amounts of Sn (-325 mesh, 99.8%, Sigma Aldrich) and red phosphorous (Anachemia) powders were milled with SPEX mill under an argon atmosphere for 1 hour to make Sn_4P_3. Electrodes consisted of a mixture of 80% by weight Sn_4P_3 powder, 10% carbon black and 10% polyimide by weight was spread onto aluminum foil with a coating bar having a 0.004 in. gap (cells for Mössbauer studies were made from coating bar with a 0.012 in. gap). Coatings were dried under vacuum at 120 °C overnight.

Electrodes were cycled in 2325 coin cells with Na disk as counter/reference electrodes. Two Celgard 2300 separators and one blown microfiber separator were used as separators. 1 M $NaPF_6$ in a solution of EC:DEC:FEC (volume ratio 3:6:1) was used as electrolyte. Cells were cycled between 1.5 V and 0.005 V; cells for electrochemical and XRD studies were cycled at C/20 rate with CCCV discharge to C/50; cells for Mössbauer studies were cycled at C/100 rate.

4.3 RESULTS AND DISCUSSION

Figure 4.1 shows the X-ray diffraction pattern and the Rietveld refinement of synthesized Sn_4P_3. The XRD pattern comprises sharp peaks characteristic of crystalline phases. All the peaks and measured lattice constants (a=b=3.976Å, c=35.3293Å, $\alpha = \beta = 90°$, $\gamma = 120°$) are in good agreement with literature data for Sn_4P_3 (JCPDS No. 20-1294).
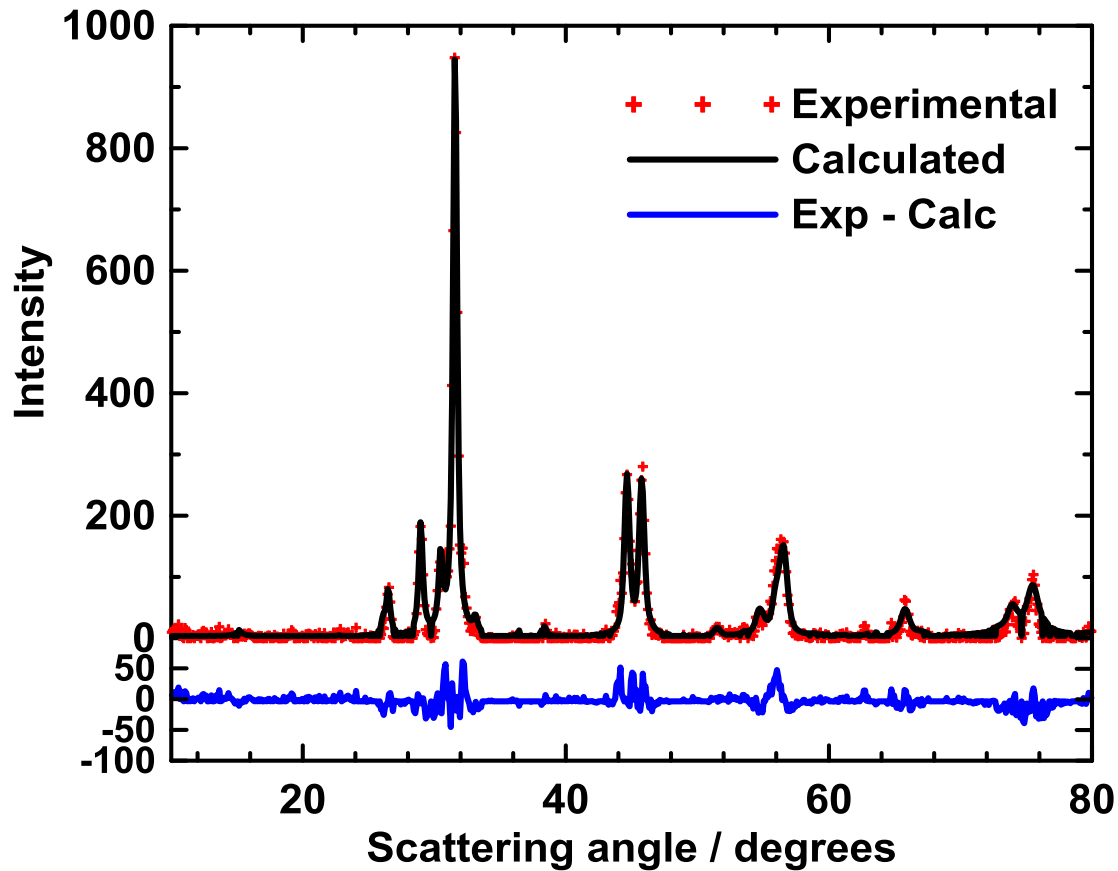
Figure 4.1 X-ray diffraction pattern and the Rietveld refinement.

Figure 4.2 shows the voltage curve of the first few cycles of a Sn_4P_3 vs Na coin cell. The capacity of the first discharge is similar to the previously reported value (>1000mAh/g); however, the cell has a higher reversible capacity of more than 900 mAh/g (in comparison with about 700 mAh/g previously reported by Qian et al. [27] and Kim et al. [28]). This may be attributed to the better binding effect of polyimide with alloy materials and to its electrochemical activity, [99] as Qian et al. [27] and Kim et al. [28] used inactive CMC and PAA as their binders, respectively.
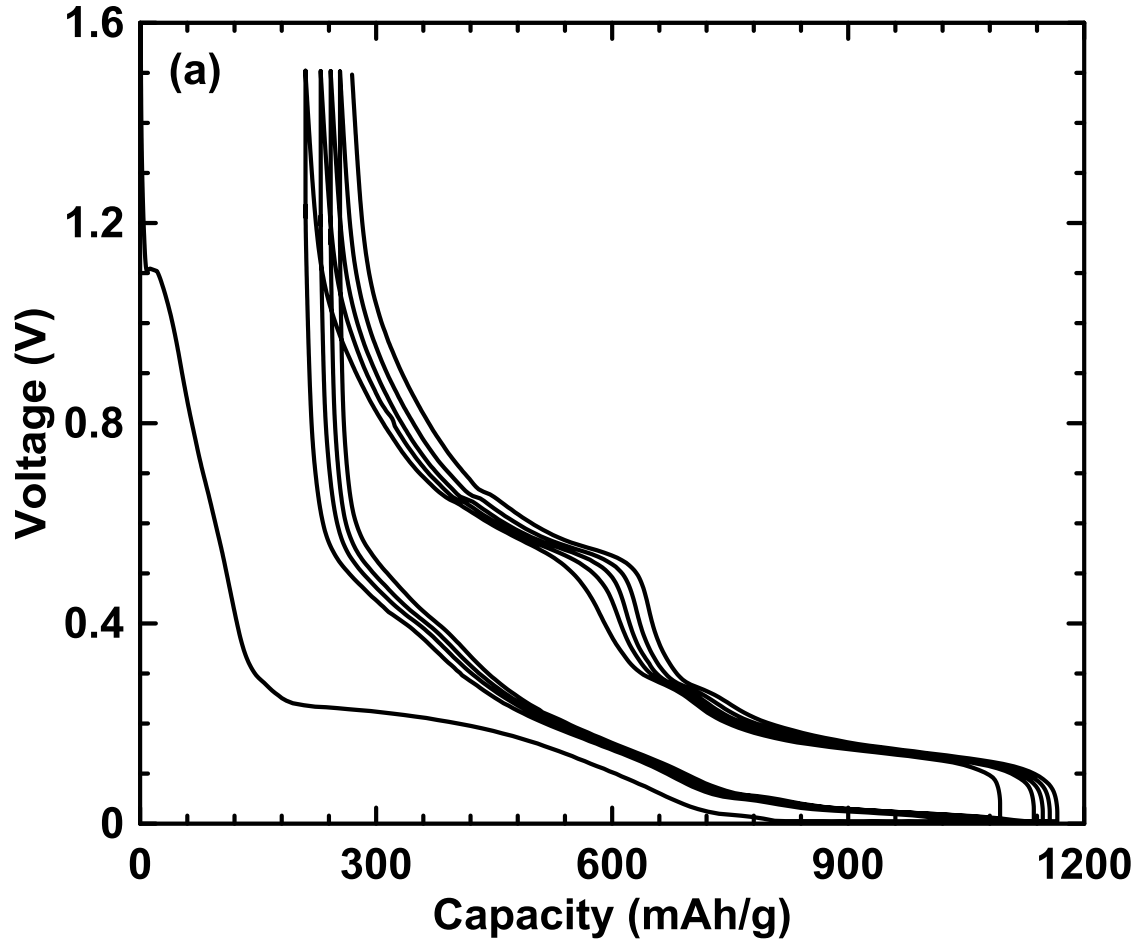
Figure 4.2 Voltage curve of Sn_4P_3 electrode cycling with Na at a rate of C/20

The discharge curve has three main features: a steep sloping plateau with a capacity of 100 mAh/g, followed by a less steep voltage plateau at about 0.3 V with a capacity of about 700 mAh/g, and finally a nearly flat plateau at very low voltage (close to 0.005V) with a capacity of 1100 mAh/g. The voltage profile during charge is also composed of three main plateaus. Figure 4.3 shows the differential capacity (dQ/dV) curve for the first two cycles. The plateaus in voltage curve can also be observed as three main peaks in the differential capacity during both discharge and charge. The hysteresis during cycling is about 0.3V.
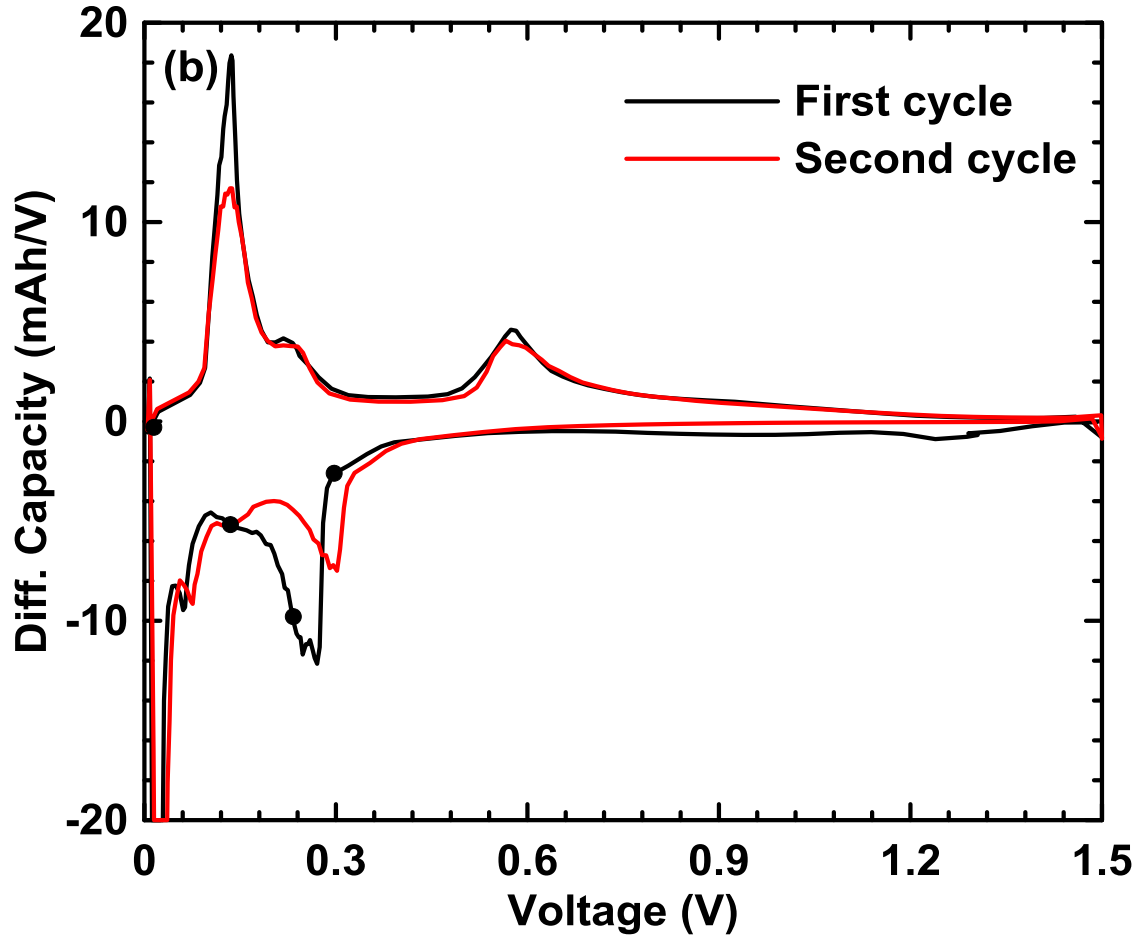
Figure 4.3 Differential capacity (dQ/dV) curve as a function of voltage for Sn_4P_3 . The black dots indicate the cut-off voltages for ex-situ XRD and Mössbauer studies.

According to studies of the sodiation of Sn by Du et al. [91] and Baggetto et al. [97], at room temperature the $Na_{0.6}Sn$ phase forms at about 0.4 V vs. Na+/Na, Na_4Sn_4 forms at about 0.2 V vs. Na+/Na, Na_5Sn_2 forms at about 0.1 V vs. Na+/Na and $Na_{15}Sn_4$ forms at a voltage near 0 V. This data can be used to predict which Sn-Na phases could be present at different cut-off voltages in the sodiation process of Sn_4P_3. Figure 4.4 shows the ex-situ XRD patterns of tin phosphide electrodes at different cut-off voltages. Upon sodiation of Sn_4P_3 below 0.3 V a rapid amorphization process initially occurs and at 0.24 V a broad peak corresponding to Na_4Sn_4

appears at about 16°. This agrees with the findings Kim et al. [28] Similar behavior has also been observed for the lithiation of Sn_4P_3.[98] After further discharging the cell to 0.135 V, peaks from Sn_4P_3 could no longer be observed, while a new broad peak at about 35.8° corresponding to Na_5Sn_2 appeared.

Figure 4.5 shows the XRD pattern measured at 0.005 V of fully sodiated Sn_4P_3 in detail. The pattern may be deconvoluted into contributions from Na_3P, Na_5Sn_2 and $Na_{15}Sn_4$. All of the above interpretations are in accordance with the voltage-phase data from Du et al.[91] and Baggetto et al.[97] However, the XRD patterns are broad and the peak assignments are not conclusive. It will be shown below that these peak assignments are in fact correct.
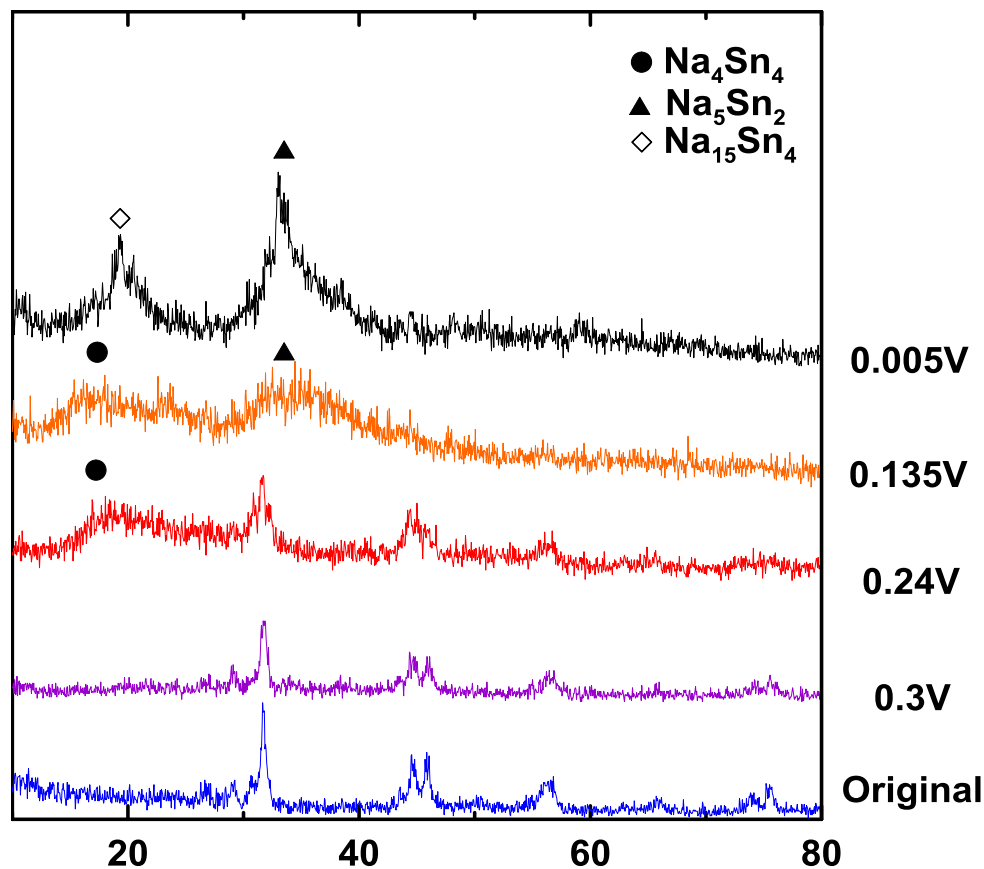
Figure 4.4 ex-situ XRD patterns of Sn_4P_3 electrodes at different cut-off voltages
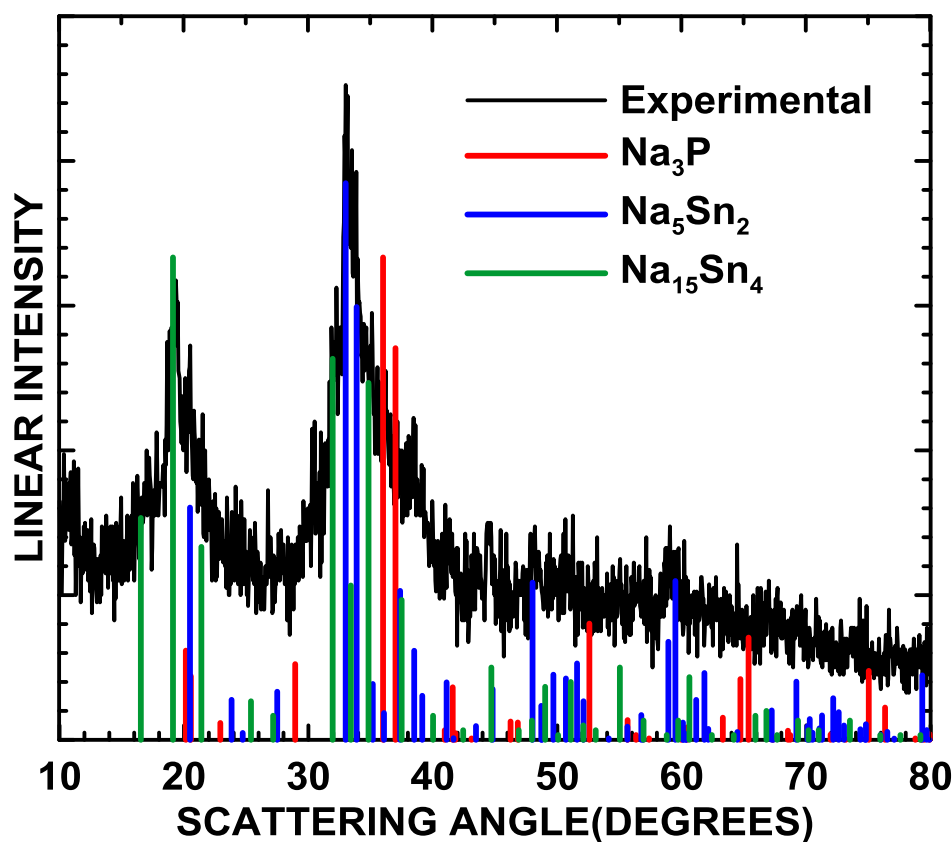
Figure 4.5 ex-situ XRD pattern of the fully discharged Sn_4P_3 electrode

Mössbauer spectroscopy was used to analyze the phase coexistence during Sn_4P_3 in a more quantitative manner than possible by XRD. Room temperature ^{119}Sn Mössbauer spectra of Sn_4P_3 electrodes measured at different stages of sodiation are shown in Figure 4.6 (a-e). The Sn_4P_3 crystal lattice contains two nonequivalent Sn sites, with a ratio of 1:1. Thus the Mössbauer spectrum of Sn_4P_3 was fitted to two doublets, as shown in Figure 4.6 (a). The center shifts of the two doublets are 2.66 and 2.67, and the intensity ratio of the two doublets is 50.2:49.8, fairly consistent with the 1:1 ratio of site occupancies. The center shift of fresh Sn_4P_3 is slightly smaller than the result reported by Häggström et al.[100] This slight difference may be caused by different

synthesis methods of Sn_4P_3, as Häggström et al heated the sample under vacuum while high-energy ball milling was used here.

The Mössbauer spectrum collected from the sample at 0.3 V was fitted to three doublets in Figure 4.6 (b), one corresponding to the formation of $Na_{0.6}Sn$ and two corresponding to the two sites of Sn_4P_3 leftover respectively. The fitting shows that the sample contains 88% Sn_4P_3 and 12% $Na_{0.6}Sn$, which means that only a small portion of Sn_4P_3 reacted with Na. This fitting agrees with the XRD pattern, where most of the Sn_4P_3 remained unchanged at 0.3 V. The Mössbauer spectrum collected from the sample at 0.24 V was fitted to four doublets in Figure 4.6 (c), corresponding to $Na_{0.6}Sn$, Na_4Sn_4, and two sites of Sn_4P_3 respectively, with ratios of 18%, 62%, 10% and 10%. The Mössbauer spectrum collected from the sample at 0.135 V was fitted to two doublets in Figure 4.6 (d): Na_4Sn_4 and Na_5Sn_2, with ratios of 33% and 67%. The Mössbauer spectrum collected from the fully discharged sample in Figure 4.6 (e) was fitted to two doublets, each representing Na_5Sn_2 and $Na_{15}Sn_4$ respectively. The ratios of the two compounds are 61% and 39%. In Figure 4.6 (e), the overall center shift of the fully discharged Sn_4P_3 (2.24mm/s) is more positive compared with the fully sodiated pure tin (2.15mm/s reported by Du et al. [91] and 2.18mm/s reported by Baggetto et al.[97]). This indicates an incomplete sodiation of Sn_4P_3, even though the cell was discharged to 0.005V. This might have resulted from the low kinetics. For each sample, the capacity of each compound can be calculated from the area ratio obtained from the fits of Mössbauer spectra. For example, at 0.135 V, the capacity used in the formation of 33% Na_4Sn_4 can be calculated as follows:

$$Capacity = r\frac{nF}{M}m = 37\% \times \frac{1\times26801\ mAh/mol}{118.7\ g/mol} \times 83.634\% = 69.869\ mAh/g \qquad (4.1)$$
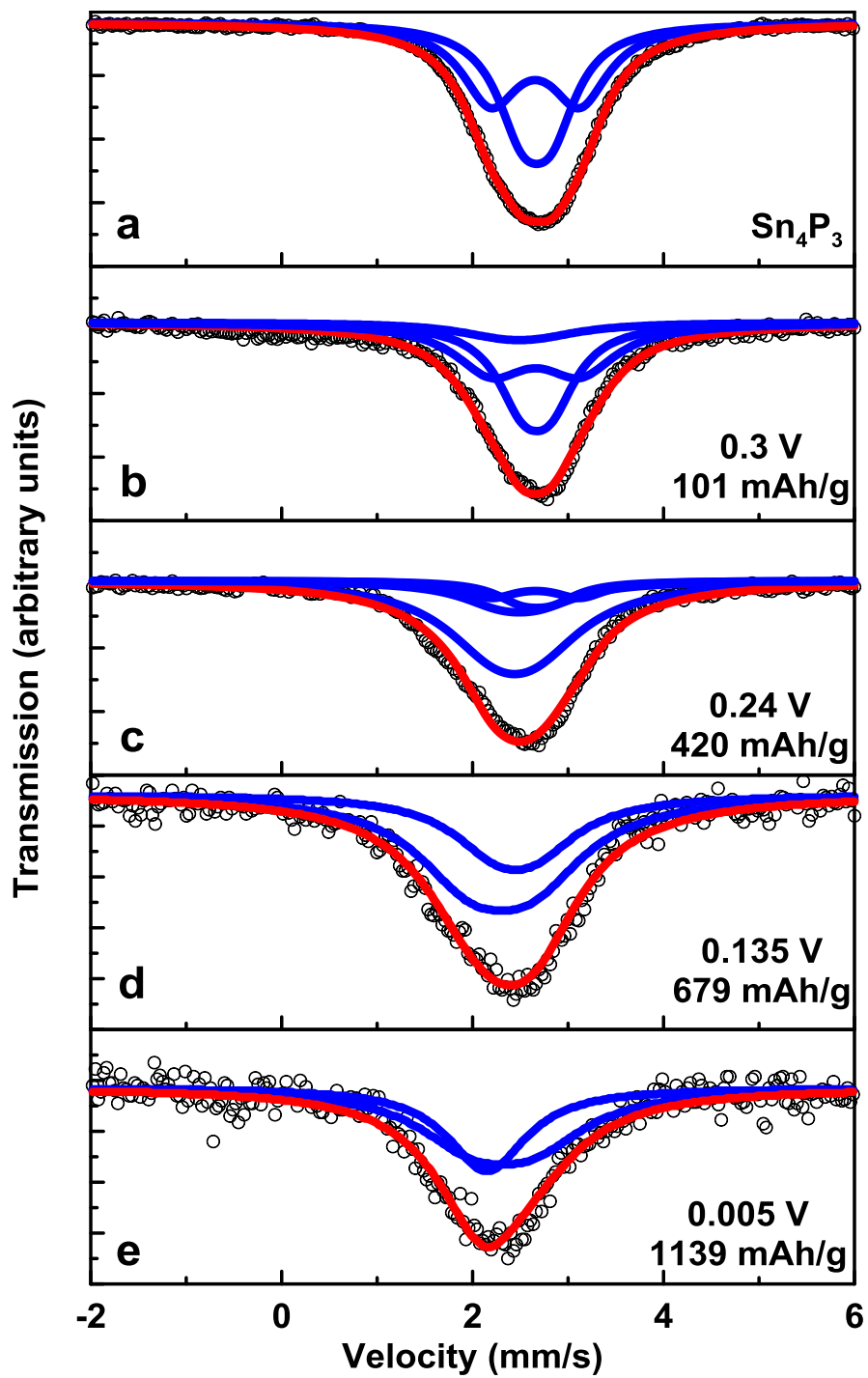
Figure 4.6 ex-situ Mössbauer pattern collected at different cut-off voltages: (a) Original Sn_4P_3 (b) 0.3 V (c) 0.24 V (d) 0.135 V (e) 0.005V The inset shows the cut-off voltage on differential capacity curve pattern for each sample.

where r is the area ratio from the fitting of Mössbauer spectrum, which is 33% in this case. F is the Faraday constant (F = 96485 coulomb/mol = 26801 mAh/mol), n is the number of the electrons transferred for each mole of Sn in the formation of Na_4Sn_4, which is 1. M is the molecular mass of Sn, 118.7 g/mol; and m is the percentage by mass of Sn in Sn_4P_3, which is 83.634%. Using the same formula, the capacity used in the formation of Na_5Sn_2 can be calculated as well. The formation of Na_xP and SEI are responsible for rest of the capacity. Using this method the distribution of the capacity can be calculated as a function of voltage. The area ratios of different phases and the capacity distribution of each sample are summarized in Table 4.1. Uncertainties in the relative area are given in (). These results will be discussed in terms of the *ex-situ* observations below. It can be clearly seen that the sodiation of Sn and P occurred at the same time.

Table 4.1 Relative Area and capacity distribution derived from Mössbauer fitting result

Materials	Relative Area	δ (mm/s)	Δ (mm/s)	Γ (mm/s)	Capacity (mAh/g)
Original Sn_4P_3		2.67			0
$Sn_4P_3^{site1}$	50%	2.67	0.32	0.32	0
$Sn_4P_3^{site2}$	50%	2.66	0.93	0.37	0
Sample at 0.3 V		2.66			101
$Sn_4P_3^{site1}$	44(2)%	2.67	0.31	0.33	0
$Sn_4P_3^{site2}$	44(3)%	2.66	0.93	0.46	0
$Na_{0.6}Sn$	12(4)%	2.49	0.36	0.61	14(5)
Na_xP+SEI					87
Sample at 0.24 V		2.51			420
$Sn_4P_3^{site1}$	10(1)%	2.67	0.31	0.33	0
$Sn_4P_3^{site2}$	10(1)%	2.66	0.93	0.32	0
$Na_{0.6}Sn$	18(1)%	2.49	0.41	0.51	20(1)
Na_4Sn_4	62(1)%	2.45	0.43	0.64	119(3)
Na_xP+SEI					281
Sample at 0.135 V		2.36			679
Na_4Sn_4	37(5)%	2.45	0.42	0.57	70(10)
Na_5Sn_2	63(7)%	2.31	0.65	0.69	297(30)
Na_xP+SEI					301
Sample at 0.005 V		2.24			1139
Na_5Sn_2	61(10)%	2.31	0.65	0.69	288(48)
$Na_{15}Sn_4$	39(10)%	2.15	0	0.50	276(67)
Na_xP+SEI					575
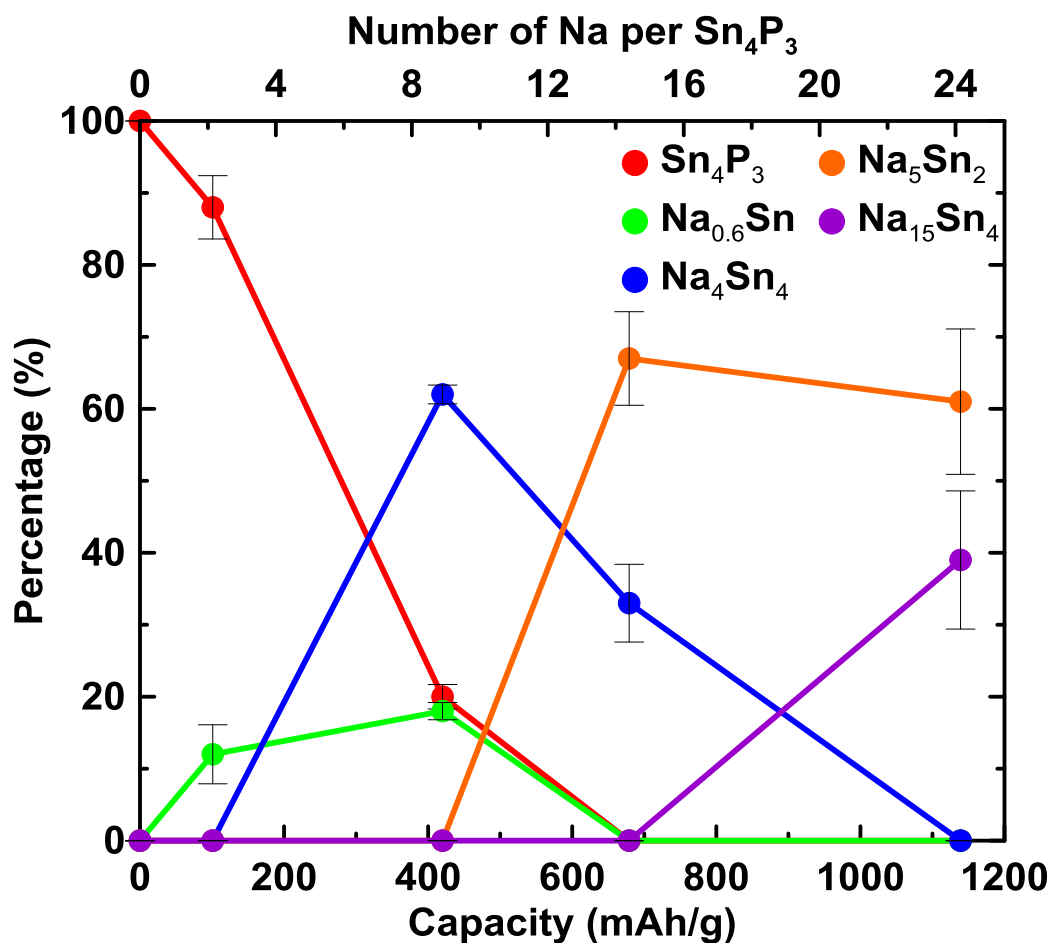
Figure 4.7 Percentage of different Na-Sn phases present in the electrode during sodiation

In Figure 4.8 the measured mean center shifts of the *ex-situ* Mössbauer spectra shown in Figure 4.6 are plotted as a function of the Na/Sn atomic ratio. For comparison, this ratio is also plotted for Na insertion into pure Sn, as reported by Du et al. [91] Both Sn and Sn_4P_3 show a trend of decreasing center shift with increasing sodiation. The Na-Sn system has a linear dependence of the center shift on the Na/Sn ratio. This decreasing center shift results from valence electrons being donated to the conduction band and additionally a reduction in the number of Sn-Sn bonds as the Na content is increased. [91] In Figure 4.8, the center shifts of Sn_4P_3 are always greater than

those of Sn, for a given Na/Sn ratio. This is expected, since the sodium that reacts with any P

during sodiation has no effect on Sn regions or their center shift. Therefore, when the same

amount of sodium and active materials reacted, the magnitude of the deviations in the center shift

in the Na–Sn_4P_3 system is always smaller than the Na–Sn system.
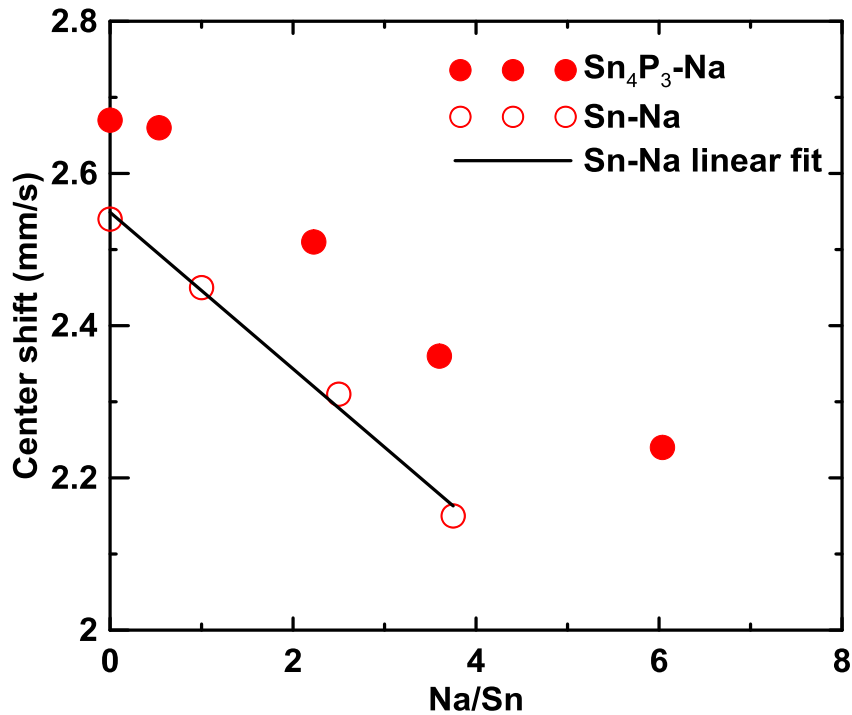
Figure 4.8 Center shifts plotted versus the Na/Sn fraction during sodiation of Sn_4P_3. The center

shifts for the sodiation of pure Sn are also shown. A linear fit was added to the pure Sn data as a

guide to the eye.

In order to correct for this effect, the measured mean center shifts are also plotted in

Figure 4.9 as a function of the Na'/Sn atomic ratio, where the Na' is the amount of sodium that

has reacted with tin only, as derived from the Na-Sn alloy content measured by Mössbauer

spectroscopy (listed in Table 4.1). By this method the amount of Na reacting with P is not

considered, and now the Sn_4P_3 center shifts are very close to those for Na-Sn alloys for high Na'/Sn contents (Na'/Sn > 1). However, the center shifts of Sn_4P_3 are higher than those for Na-Sn alloys at low Na contents (Na'/Sn < 1). This is because at the early stages of sodiation, unreacted Sn_4P_3 still exists in the electrode, and thus the overall center shift is more positive because of Sn-P interactions. As the sodiation progresses, Sn_4P_3 becomes consumed and is progressively replaced by Na-Sn phases and the center shift of the Sn_4P_3 electrode and Sn begin to converge. When Na'/Sn ≈ 1 all the Sn_4P_3 has reacted with Na and all the Sn is now in the form of Na-Sn phases. At higher Na contents the Sn_4P_3 and Sn electrode center shifts become identical.
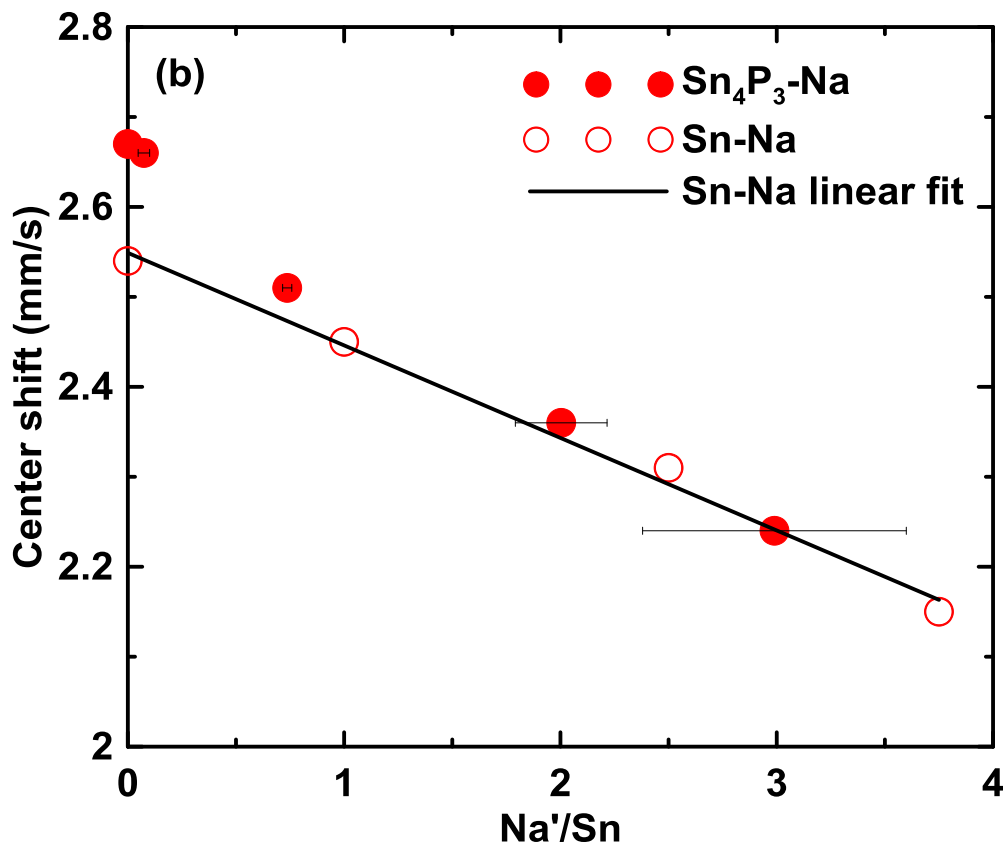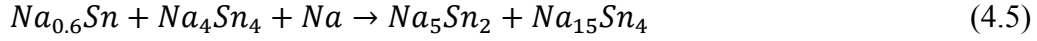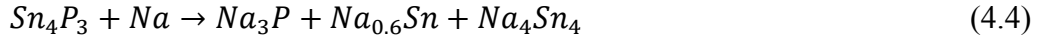

Figure 4.9 Center shifts plotted versus the Na'/Sn fraction (as described in the manuscript) during sodiation of Sn_4P_3. The center shifts for the sodiation of pure Sn are also shown. A linear fit was added to the pure Sn data as a guide to the eye.

By combining the results from XRD and Mössbauer spectroscopy, it can be concluded that as the sodium is inserted into Sn_4P_3, they react according to the following equations:

$$Sn_4P_3 + Na \rightarrow Na_3P + Na_{0.6}Sn + Na_4Sn_4 \tag{4.4}$$

$$Na_{0.6}Sn + Na_4Sn_4 + Na \rightarrow Na_5Sn_2 + Na_{15}Sn_4 \tag{4.5}$$

It should be noted that neither equation (4.4) nor equation (4.5) are not balanced equations and are only meant to show the reactants and products. Here Na first reacts with Sn_4P_3 to form Na_3P, $Na_{0.6}Sn$, and then Na_4Sn_4, according to equation (4.4). After this, the Na-Sn phases react with Na to make Na_5Sn_2 and $Na_{15}Sn_4$, according to equation (4.5). A similar process was also suggested by Pérez-Vicente et al.,[98] when Sn_4P_3 reacted with Li in a electrochemical cell: the lithiation of Sn starts almost immediately upon lithiation, and then then the lithiation of Sn and P take place simultaneously.

4.4 CONCLUSION

Sn_4P_3 was prepared using high-energy ball milling, and Sn_4P_3 composite electrodes were cycled with Na in half cells. These electrodes were collected at different cut-off voltages and were studied by ex-situ X-ray diffraction and Mössbauer spectroscopy. The results suggest that upon sodiation, Sn and P begin to react with sodium simultaneously, resulting in the formation of Na_3P and $Na_{0.6}Sn$, and Na_4Sn_4, phases. After further sodiation these Na-Sn phases react with more sodium and eventually form $Na_{15}Sn_4$. These findings are consistent with the behavior of Sn_4P_3 in Li cells. This provides a good example of how Mössbauer spectroscopy can provide insight into the mechanism of metal alloying reactions in metal ion cells.

CHAPTER 5 TRANSITION METAL PHOSPHIDES AS ANODE MATERIALS FOR SODIUM-ION BATTERIES

5.1   INTRODUCTION

Phosphorus and phosphorus-based materials are attractive anode materials for sodium ion batteries as they offer high theoretical capacity at low voltages.[87] Phosphorus has anomalously low volume expansion for sodium insertion compared to other metal alloys. The theoretical volumetric capacity of phosphorus exceeds that of metallic sodium.[87] However, this expansion rate is still large for electrode materials, which can leads to poor cycling performance. Using phosphides instead of phosphorus can reduce the volume expansion and may provide a solution to this. In a transition metal phosphide (M-P), M is inactive towards sodiation while P is active. During sodiation, a conversion reaction occurs, in which M metal and Na-P phases are formed. If we assume all the phosphorus reacts to form Na_3P, then this conversion mechanism can be represented by the reaction:

$$M_a X_b + (bc)Na \rightleftarrows aM + bNa_c X \qquad (5.1)$$
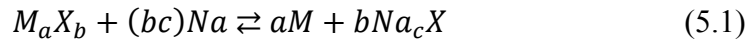
where the arrows in the above equation are meant to represent a reversible, but non-equilibrium, process. Since M does not participate in reaction with sodium, it dilutes the volume expansion.

High-energy ball milling is known to be an effective method for the synthesis of nanostructured materials. This technique has been used extensively by researchers to study several transition metal phosphides as anode materials for lithium ion batteries, such as TiP_2,[101] ZnP_2,[102] Cu_3P,[103] etc. During milling, samples are exposed to repetitive impacts by balls,

resulting in localized regions of elevated temperature and pressure.[104] In this process, energy is transferred to powder samples and alloys can be produced from elemental powders.

Recently, Fullenwarth et al.[30] studied NiP_3 made from ball-milling as anode for sodium ion batteries. NiP_3 shows a reversible capacity of more than 800 mAh/g, corresponding to about 6 Na ions per NiP_3 formula unit. Li et al.[29] have reported that ball-milled FeP has a reversible capacity of about 500 mAh/g. However, other transition metal phosphides as anode materials for sodium ion batteries have not been reported.

In this study, several 3d transition metal phosphides were synthesized by high energy ball milling and their electrochemistry as anode materials were characterized in Na-ion half-cells at different temperatures. Ex-situ XRD measurements were performed to confirm the structure change and reaction mechanism during cycling.

5.2   EXPERIMENTAL

All transition metal phosphides were synthesized via high-energy ball milling. Stoichiometric amounts of elemental transition metal powders (Titanium powder, -325 mesh, 99%, Sigma Aldrich; Manganese powder, 99.9%, Sigma Aldrich; Cobalt powder, 1.6um, 99.8%, Alfa Aesar; Copper Powder, -325 mesh, 99%, Alfa Aesar; Zinc Powder, -100 mesh, 99.9%, Alfa Aesar) and red phosphorus powder (Anachemia) were milled under Ar atmosphere for different time spans with a high energy ball mill (SPEX Model 8000-D, Spex Certiprip, Metuchen, N.J.). Ball milling was carried in a 65mL hardened steel ball-milling vials with 0.5 in. hardened steel balls at a ball-to-power ratio of 20:1(usually around 2g of sample powders and 40g of balls were

used). During the milling process, the milling vial temperature increased to about 70°C. The milling vials were allowed to cool to room temperature before being opened in air.

Electrodes for electrochemical studies were made with active material, carbon black (Super P, Erachem Europe) and binder at a ratio of 8:1:1. Binder was either PVDF (polyvinylidene fluoride, Kynar HSV 900) or polyimide (PI-2555, HD Microsystems, 20% in N-methyl-2-pyrrolidone). These components were mixed in N-methyl-2-pyrrolidone (Sigma Aldrich, anhydrous 99.5%) with two tungsten carbide balls in a Retsch PM200 rotary mill (100 rpm, 1 hour) to create a uniform slurry. The slurry was then spread onto copper foil with a coating bar having a 0.004 in. gap. The electrodes were then dried under vacuum at 120 °C overnight. 1.3 cm^2 circular electrodes were punched from the resulting coatings. Electrodes made with PI binder were heated at 300 ℃ for 3 hours in flowing Ar before being assembled into cells.

Cell assembly was carried out in an Ar-filled glove box. The electrolyte was 1M NaPF$_6$ in a solution of ethylene carbonate, diethyl carbonate and monofluoroethylene carbonate (all from BASF) with a volume ratio 3:6:1. Na foil, cold rolled from sodium ingot (Sigma Aldrich, ACS reagent grade), was used as counter/reference electrodes. Two Celgard 2300 and one blown microfiber separator (3M Company) were used as separators. Cells were cycled between 0.005 V and 1.5 V with a Maccor Series 4000 Automated Test System with a C/40 rate at 30 °C, 60 °C and 80 °C. For cells cycled at 30 °C, 2325-type coin cells were used. Conflat cells were used for cells cycled at 60 °C and 80 °C.[95]

Synthesized transition metal phosphides were characterized by XRD using a Rigaku Ultima IV X-Ray Diffractometer equipped with a Cu Kα X-ray source (Kα = 1.54 Å) X-ray tube and a scintillation detector with a diffracted beam monochromator. Cells for ex-situ XRD

measurements were opened in an Ar-filled glove box. Electrodes were carefully removed from the current collectors and rinsed with dimethyl carbonate (DMC, BASF) several times to remove any residual salt. Samples were then sealed in an air-tight X-ray sample holder described by Fielden et al.[63] (DPM Solutions, Hebbville NS) in Ar-filled glove box for ex-situ XRD measurements.

5.3   RESULTS AND DISCUSSIONS

Figure 5.1 shows the XRD pattern of synthesized metal phosphides and the milling time for each phosphide. All synthesized materials have their targeted stoichiometric phase as their majority phase, with little or no impurities, indicating that transition metal phosphides can be synthesized with high-energy ball milling in a few hours. After being exposed to air for 72 hours, these materials were characterized once again by XRD, and no change was observed in their XRD patterns, indicating the air-stability of synthesized materials.
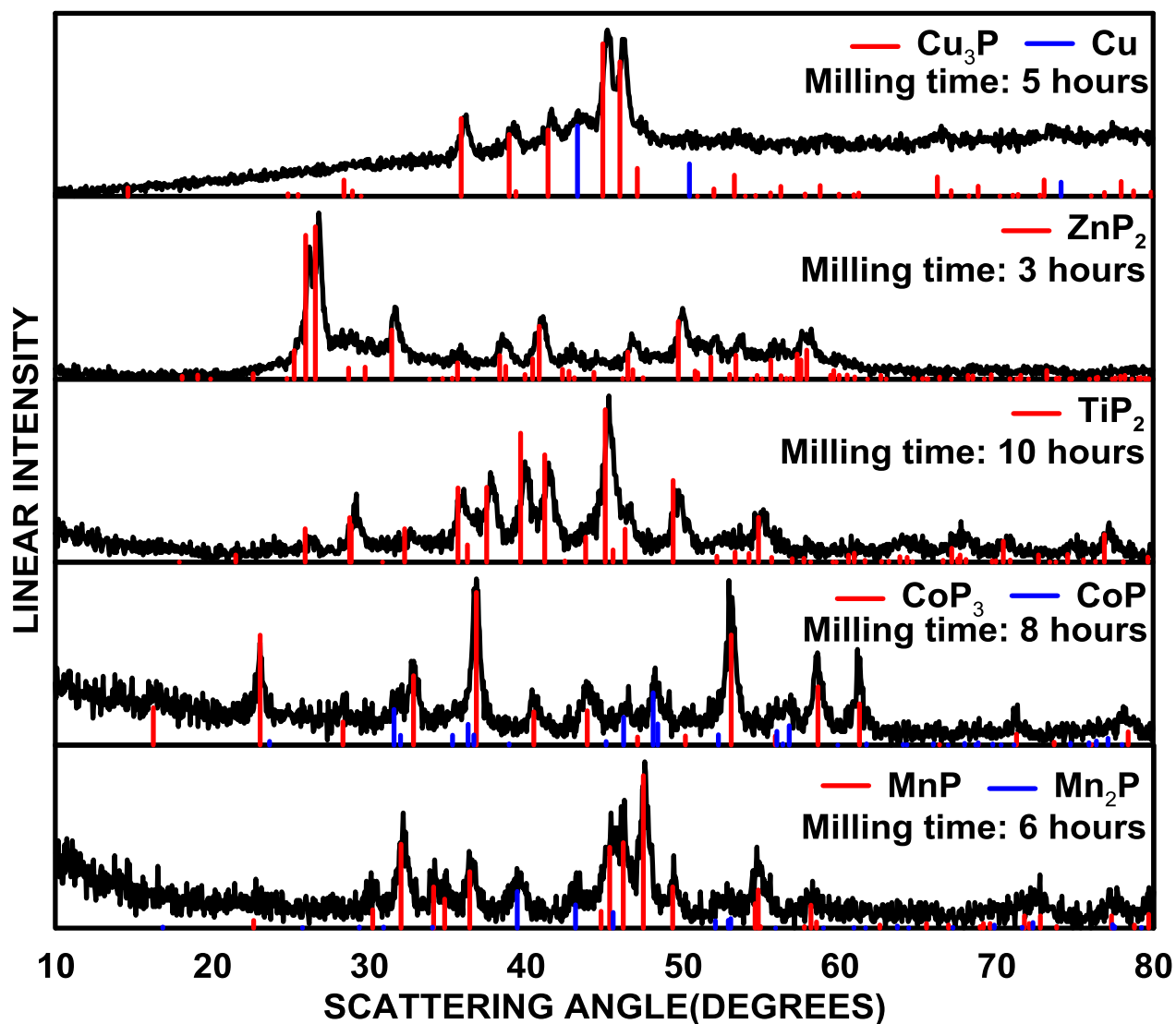
Figure 5.1 XRD patterns of all synthesized samples and reference patterns.

Figure 5.2 shows the voltage curves of all synthesized electrodes at 30°C. ZnP_2 and Cu_3P have first sodiation capacities of 830 mAh/g and 311 mAh/g, respectively, which are close to their theoretical capacities. The first sodiation capacities of TiP_2, MnP, CoP_3 are 182 mAh/g, 229 mAh/g and 325 mAh/g, respectively, much less than their theoretical values (listed in **Table 5.1**). This phenomenon of observed capacities being significantly lower than theoretical capacities is also observed in other studies on sodium ion batteries undergoing conversion reactions, possibly

due to kinetic limitations.[105]

In general, the reversible capacities are less than the theoretical capacities. This is likely due to mechanical failure of the electrode, due to the large volume changes during cycling, as will be discussed further below. The reversible volumetric capacity of these materials at full sodiation state were calculated based on the molar volume of the M, M-P and Na_3P phases, and the results are summerized in **Table 5.1**. The reversible volumetic capacities of ZnP_2 and Cu_3P are 652 Ah/L and 922 Ah/L, respectively, which are considerably higher than that of hard carbon (~450 Ah/L), while TiP_2, MnP and CoP_3 show low reversible capacities. The irreversible capacities and polarization, however, are high for all the synthesized materials, which is typical of conversion reactions.
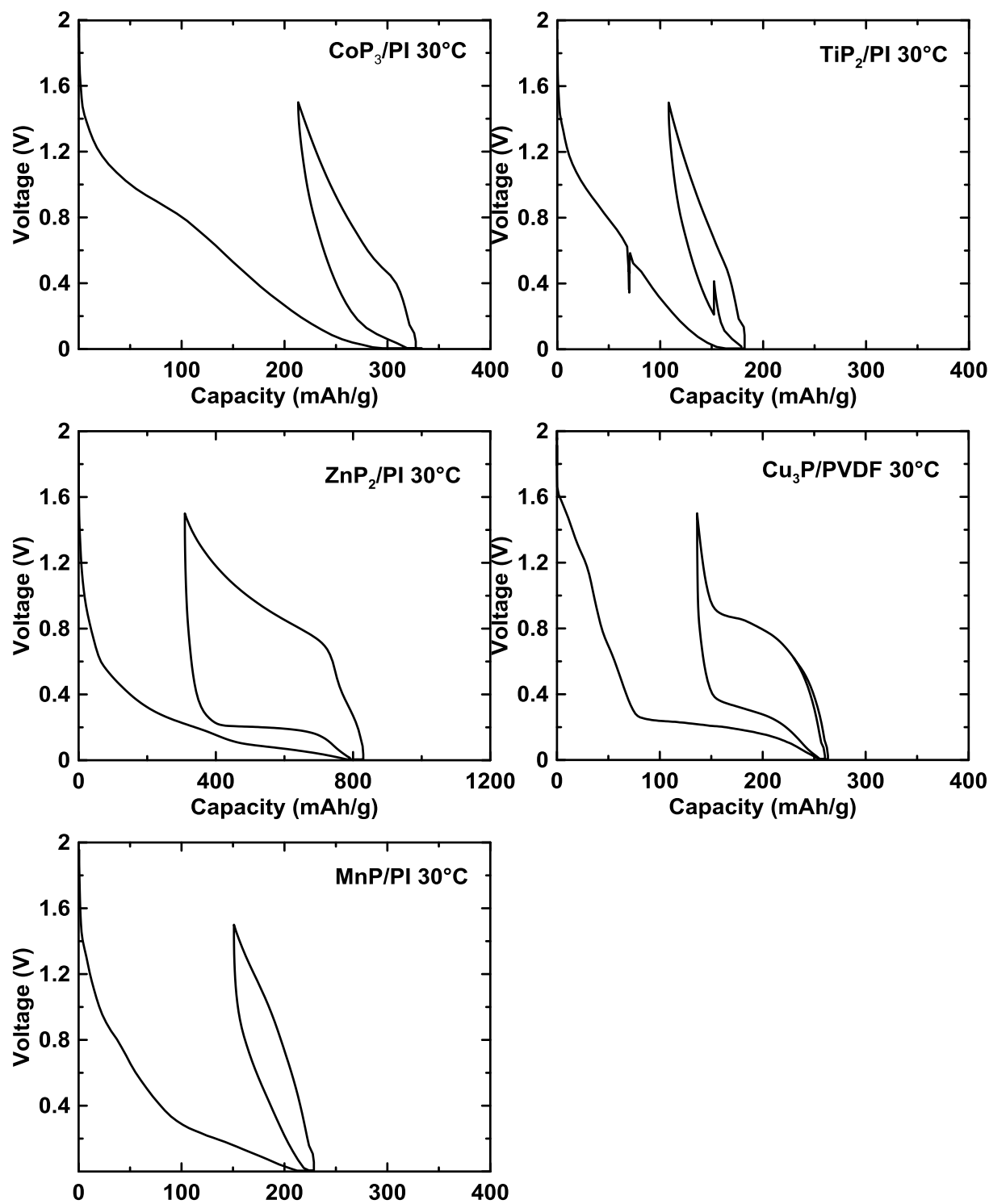
Figure 5.2 The voltage curve for all synthesized samples in Na half-cells.

Table 5.1 Specific and volumetric capacities of phosphides in Na half cells at 30°C

Materials	Theoretical capacity (mAh/g)	First discharge capacity (mAh/g)	Reversible capacity (mAh/g)	Reversible volumetric capacity at full sodiation (Ah/L)
TiP$_2$	1463.10	182	74	265
MnP	935.14	229	78	353
CoP$_3$	1587.08	325	114	387
Cu$_3$P	362.59	311	148	652
ZnP$_2$	1261.87	830	520	922

It is well known that binders play an important role in alloy electrode materials. PVDF does not chemically bond to the electrode particles or current collector. In addition, PVDF only forms polymer threads around the electrode surface, which leaves much of the electrode surface exposed to electrolyte. Severe swelling also occurs for PVDF threads when exposed to electrolyte. All these characters are detrimental to the binding effect of PVDF. Therefore, PVDF is not a good choice of binder when the electrochemical reaction is accompanied by large volume expansion.[26] **Figure 5.3** shows a comparison of the voltage curve of ZnP$_2$ using PVDF and PI binders. The first sodiation capacities are similar (~850 mAh/g) and close to the theoretical capacity of ZnP$_2$. During the first sodiation half-cycle, the volume expansion would keep the particles in good contact. Therefore, during the first sodiation half-cycle, even a poor binder can achieve a capacity close to full sodiation. However, during desodiation, the active materials can become disconnected as they contract. It is observed that the first reversible capacity of ZnP$_2$ in PVDF binder is much less than ZnP$_2$ in a PI binder (~500 mAh/g in

comparison to ~100 mAh/g), indicating the better binding effect of PI than PVDF in this case.
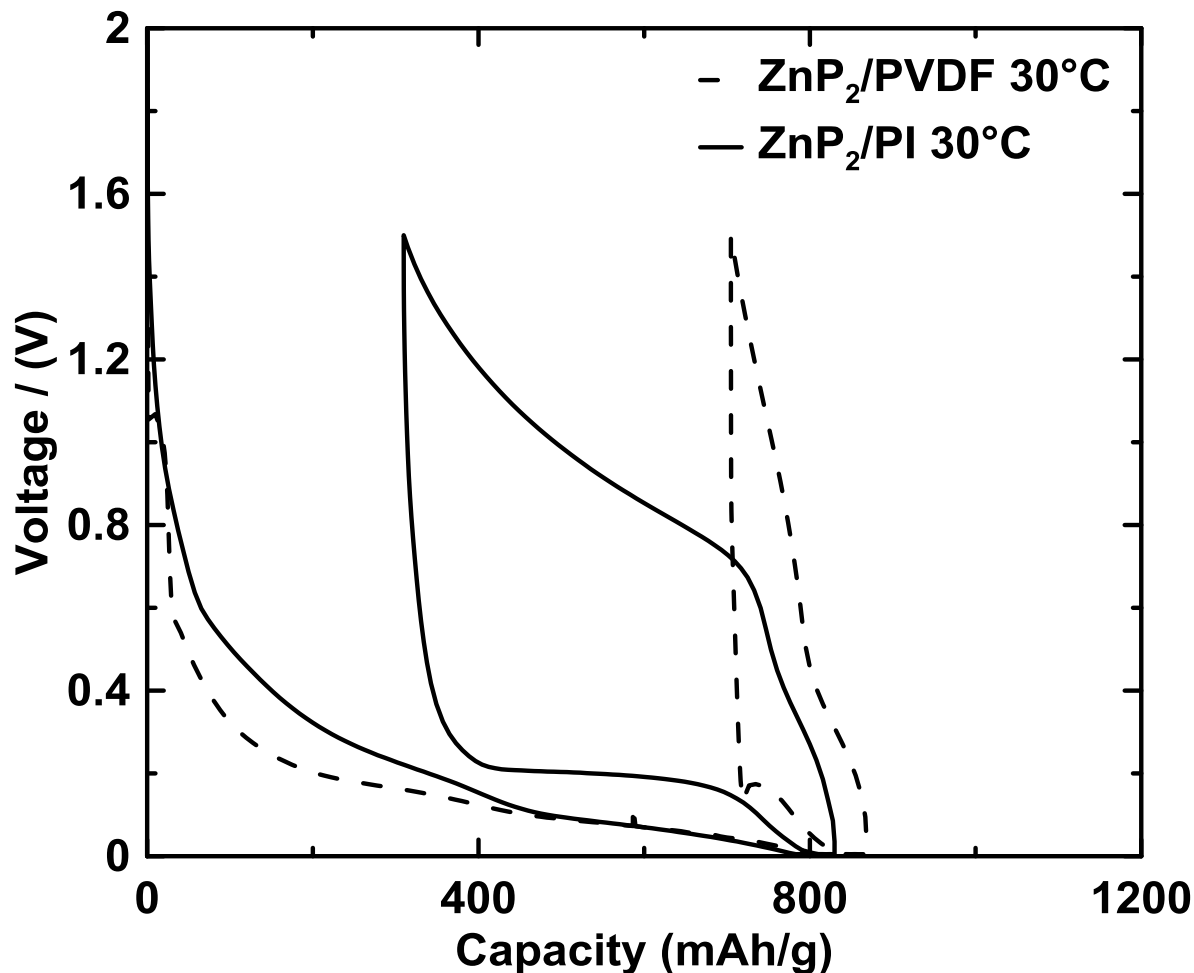
Figure 5.3 Voltage curve for ZnP_2 with different binders

Increasing the cell-operating temperature usually leads to better diffusion, resulting in larger reversible capacity and lower polarization. Since all the materials in this study suffer from high irreversible capacity and polarization, the performance of phosphides at elevated temperature was studied, in hope of achieving batter electrochemical behavior. **Figure 5.4** and **Figure 5.5** shows the comparison of ZnP_2 and Cu_3P cells operating at 30 °C and 60 °C. It can be seen that the first discharge capacity of ZnP_2 electrode with PI binder at 60 °C (~1100 mAh/g) almost reaches its theoretical capacity. However, the subsequent recharge capacity remains

similar to the cell operated at 30 °C (~500 mAh/g).
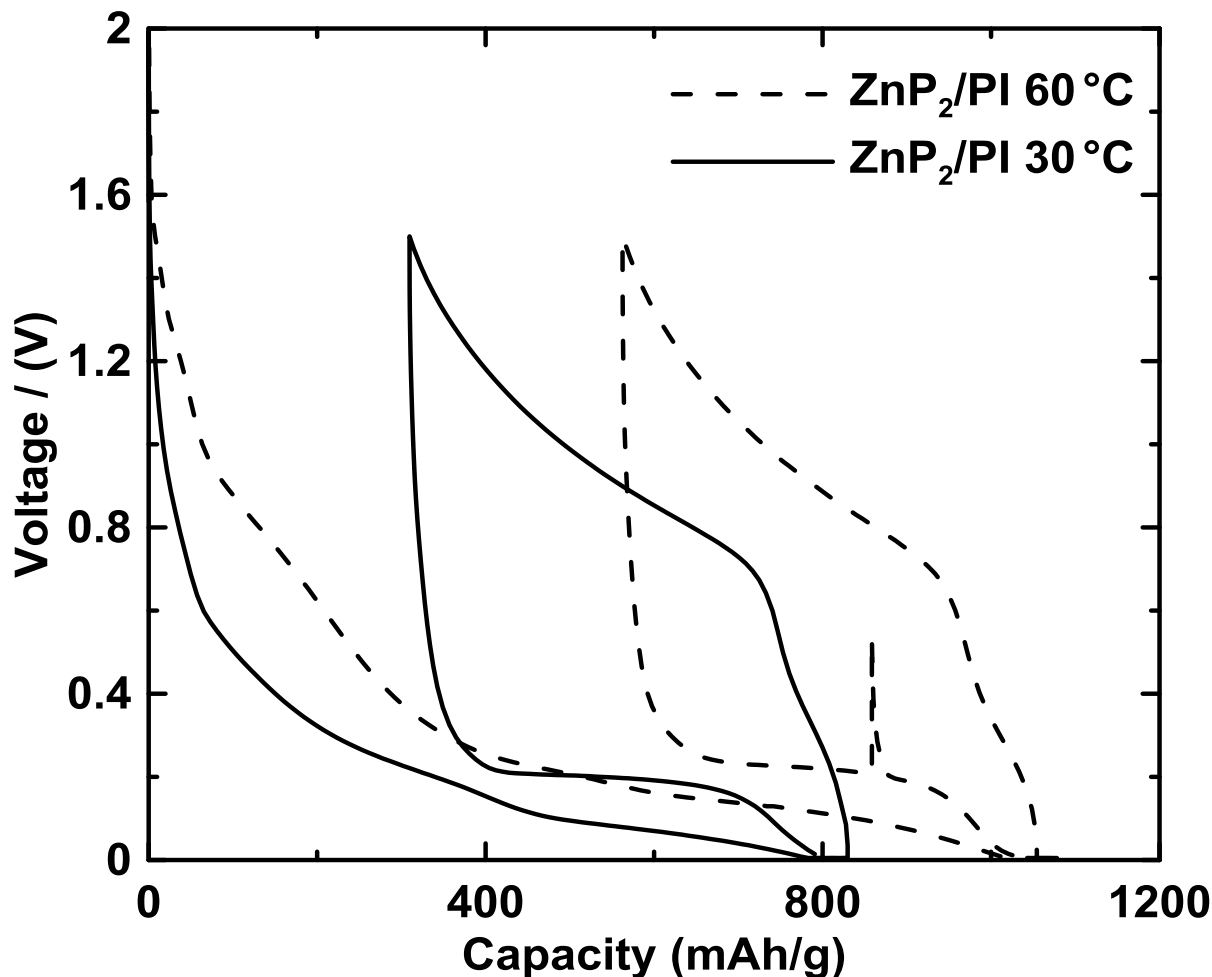
Figure 5.4 Voltage curve for ZnP$_2$ electrode with PI binder operating at different temperatures

As shown in Figure 5.5, a first discharge capacity far exceeds its theoretical capacity is observed at 60 °C for Cu$_3$P. A long plateau with a capacity of about 400 mAh/g was observed at about 1.4 V. However, again, the recharge capacity remains similar to the cell at 30 °C and the long plateau at ~1.4 V is irreversible. The reason for the abnormal phenomenon that discharge capacity being much higher than that of theoretical capacity is unknown, possibly due to accelerated electrolyte reaction at high temperature catalyzed by phosphides.

For TiP$_2$, as shown in Figure 5.6, cells were cycled at 30 °C, 60 °C and 80 °C,

respectively. The first few cycles for each temperature were shown below. It can be seen that as the operating temperature increases, the first charge capacity and the reversible capacity both increase, while the hysteresis decreases. At 80 °C, a reversible capacity of ~260 mAh/g was observed, which is more than 3 times of that at 30 °C. The volumetric capacity corresponds to ~660 Ah/L. The hysteresis was reduced to ~0.3 V. Even though the capacity is still much less than its theoretical capacity, a huge improvement in performance was observed at high temperature. However, on the other hand, the voltage curve has more slippage to higher capacities as the temperature increases, indicating electrolyte decomposition reactions or other side reactions that occur in the cell. Therefore, it might be interesting to lower the cell temperature to 30 °C after cycling at 80 °C to see if the cell can maintain the improved reversible capacity while reducing voltage slippage. The voltage curve of TiP_2 also looks different than ZnP_2 and Cu_3P, it is possible that a mechanism other than conversion (such as intercalation) is taking place.

Overall, it was observed that increasing the temperature has different effect for different metal phosphides. For some materials, such as ZnP_2 and Cu_3P, increasing the cycling temperature can only increases the first discharge capacity, but has a little effect on reversible capacity. Therefore the increasing of the first discharge capacity may come from the enhanced electrolyte decomposition and other side reaction at elevated temperature. For TiP_2, increasing the temperature greatly improves the performance. At 80 °C, the reversible capacity of TiP_2 was more than 3 times of that at 30 °C. The hysteresis was also reduced to ~0.3V.
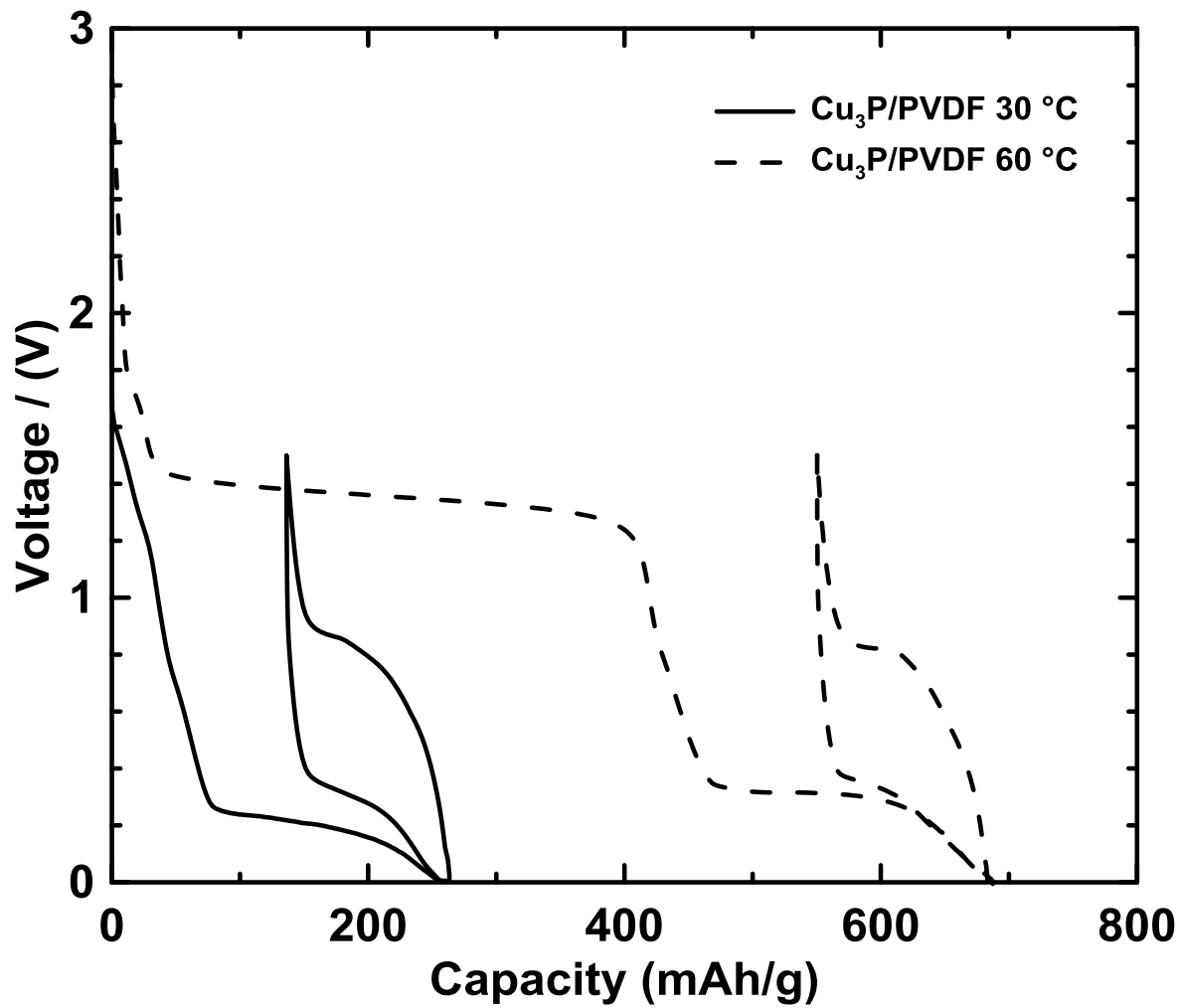
Figure 5.5 Voltage curve for Cu$_3$P operating at different temperatures
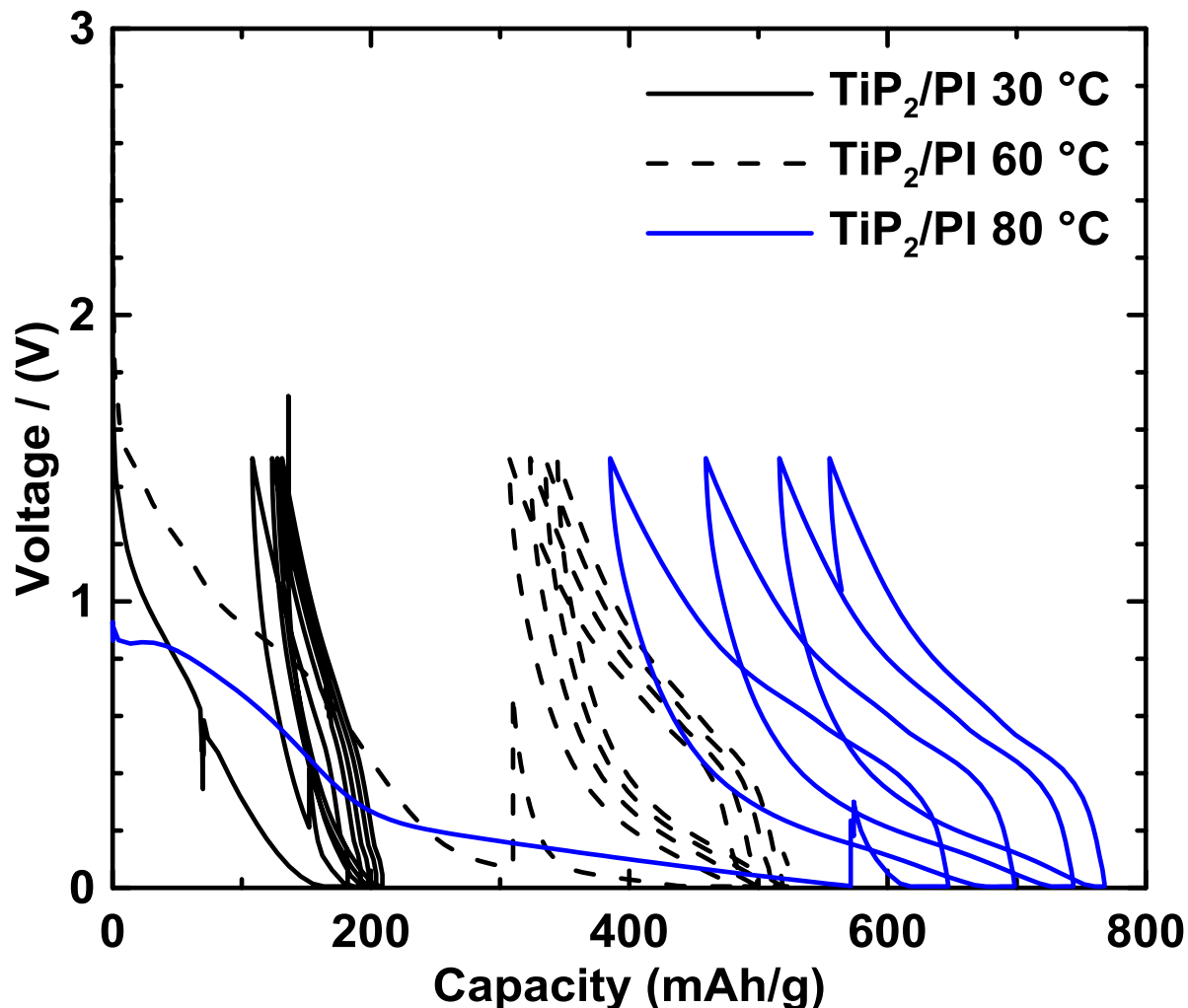
Figure 5. 6 Voltage curve for TiP$_2$ operating at different temperatures

In a conversion reaction, M-P undergoes a displacement reaction and forms Na-P phases and M metal upon sodiation, according to equation (5.1). To confirm the mechanism of the electrochemical sodiation of phosphides, ex-situ XRD measurements were carried out. The ex-situ XRD patterns of fully sodiated (discharged to 0.005V) and desodiated (discharged to 0.005V then charged to 1.5 V) Cu$_3$P with PVDF binder at 30 °C are shown in **Figure 5.7**. It can be seen from Fig. 4 that the peaks from Cu$_3$P decrease in intensity, while the peaks from Cu increase in intensity. No Na-P phases are observable in the XRD pattern and are likely

amorphous. The amorphization behavior is common for conversion reactions.[105] After fully charging, the XRD pattern has increased in intensity in the regions where Cu_3P peaks should be and the Cu peak has decreased in intensity. This could be attributed to the formation of amorphous Cu_3P, confirming the reversible conversion reaction.
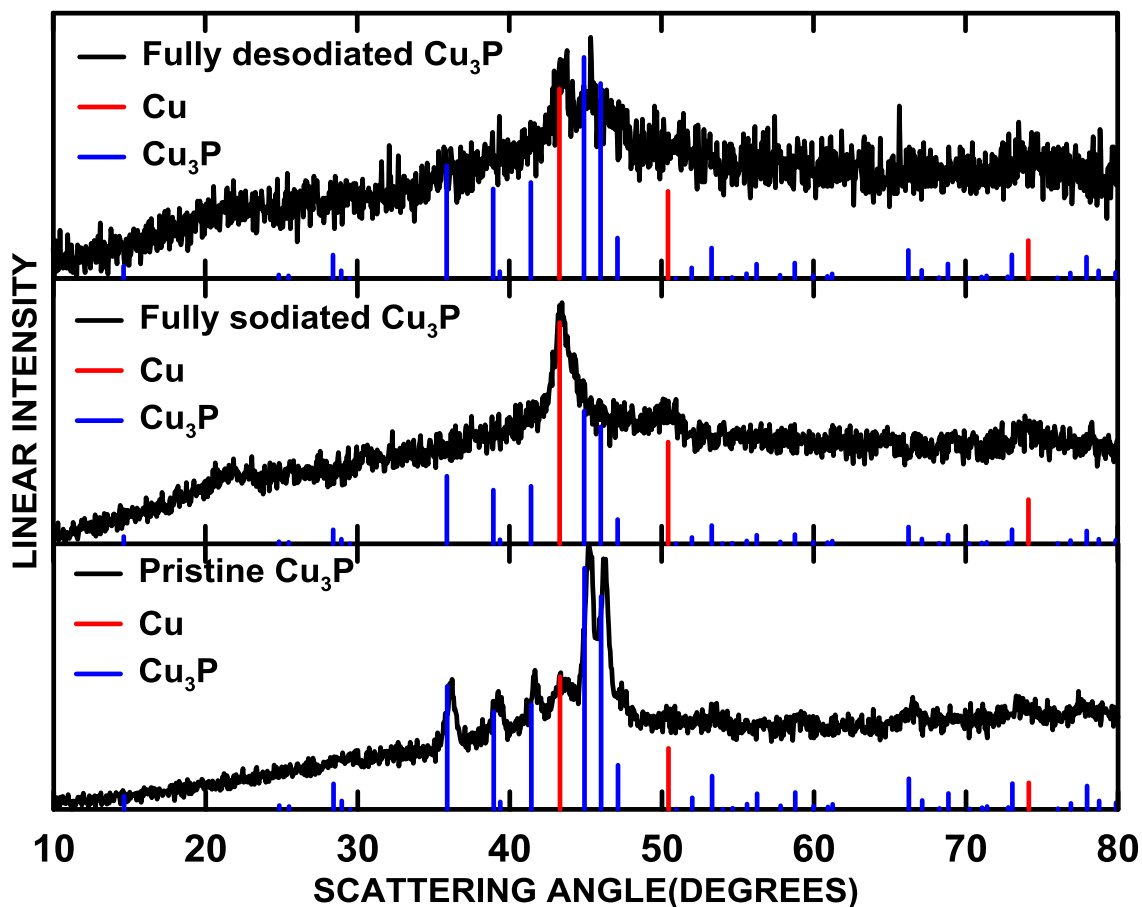
Figure 5.7 Ex-situ XRD patterns for pristine Cu_3P, fully sodiated Cu_3P and desodiated Cu_3P

For materials that have a first discharge capacity much less than their theoretical capacity, such as CoP_3, the ex-situ XRD shows almost no change before and after first sodiation (cell cycled at 30°C with PVDF binder), as shown in Figure 5.8. This is expected, since the majority of the electrode is still unreacted CoP_3 after the first sodiation. According to the ratio of first discharge capacity and theoretical capacity, only less than ~20% of the pristine material is

consumed during the first sodiation. Therefore, the structure is still dominated by pristine material, as shown in Figure 5.8.
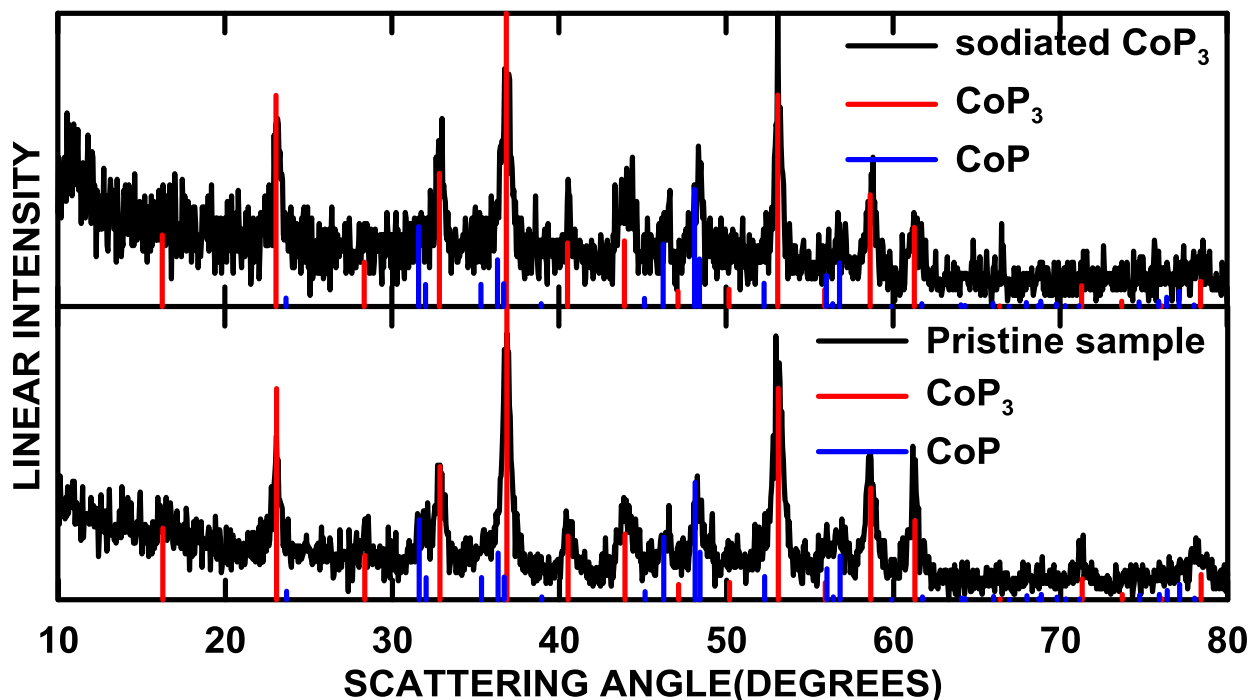
Figure 5.8 Ex-situ XRD patterns for fully sodiated and pristine CoP$_3$

The cycling performanc of metal phosphides were evaluated for all the materials with different binders at 30 °C or 60°C. It was found that the higher the volumetric capacity, the poorer the cycling performance. For ZnP$_2$, which shows the highest volumetric capacity during the first cycle, a severe capacity fade is observed. As shown in Figure 5.9, the capacity fades quickly and after 5 cycles the capacity retained is only less than 200 mAh/g. The coulombic efficiency was poor as well. The poor cycling performance might be due to the high capacity of ZnP$_2$, which lead to a high volumetric change during cycling. Materials with less capacity, and thus, less volumetric change were studied for comparison. The cycling performance of Cu$_3$P at 30 °C was shown in Fig 5.10. A better cycling performance than ZnP$_2$ is observed. After 50 cycles the capacity retention is about 50%. For CoP$_3$, the cycling performance when different

temperatures and binders were used is shown in Fig 5.11. The volumetric capacity of CoP_3 is much less than its theoretical capacity and less than that of Cu_3P and ZnP_2. However, the best cycling performance was observed among the three. At 30 °C, the electrodes with both PI and PVDF binder show good cycling performance. The capacity of electrode with PI binder is slightly higher than that of PVDF binder. The electrode with PVDF binder has a capacity retention of ~80% after 50 cycles. The electrode with PI binder shows higher capacity than its initial capacity after 50 cycles. This might be due to more active materials becoming accessible to electrochemical reaction during repetitive cycling. At 60 °C, electrodes with PI and PVDF binder have similar first cycle capacities. However, for PVDF binder, at 60°C the fade was much more dramatic than that at 30°C. While for PI binder, a similar capacity increasing behavior was observed during the 50 cycles. Overall, CoP_3 has the best cycling performance, compared with ZnP_2 and Cu_3P.
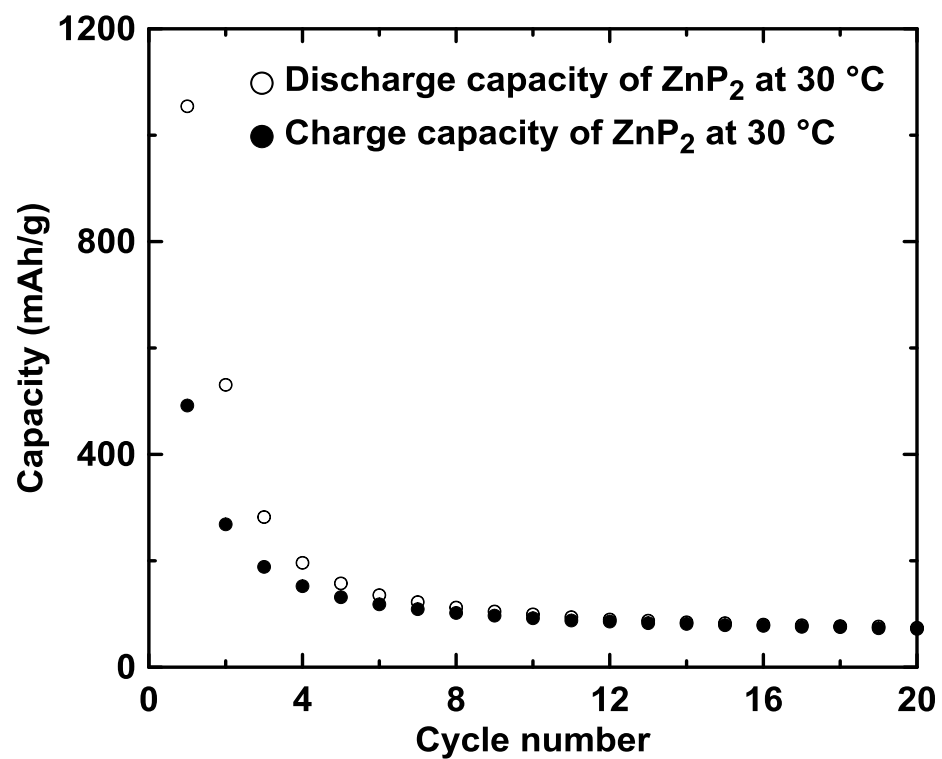
Figure 5.9 Cycling performance of a ZnP$_2$ electrode with PI binder at 30 °
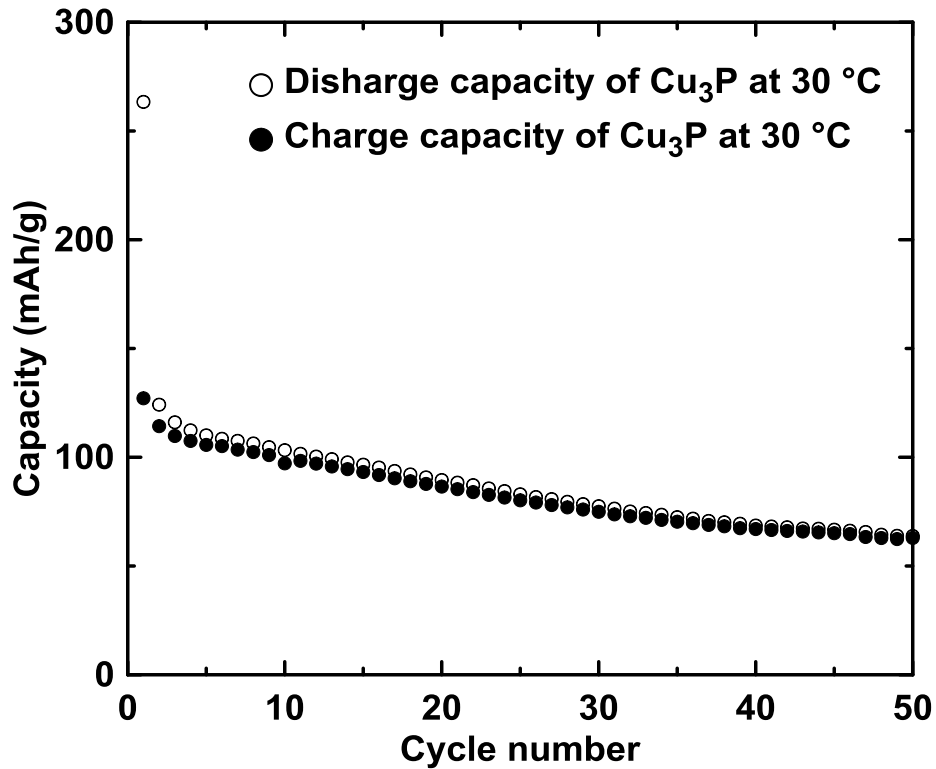
Figure 5.10 Cycling performance of a Cu₃P electrode with PVDF binder at 30 °
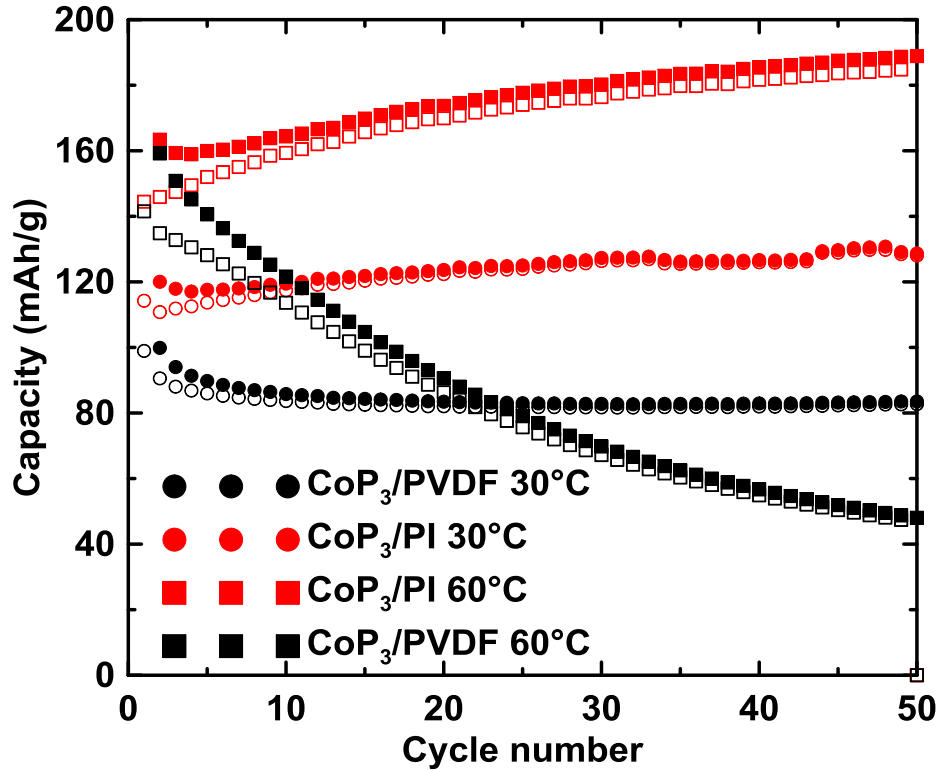
Figure 5.11 Cycling performance of CoP₃ electrodes at 30 °C and 60 °C with different binders

5.4   CONCLUSION

Transition metal phosphides were made from mechanical ball-milling and characterized by XRD. Targeted stoichiometric phase as majority phase was observed. Conversion reactions occur during the sodiation/desodiation of the materials. Most of these materials have lower capacity than their theoretical capacities. ZnP_2 and Cu_3P show volumetric capacities that exceed that of hard carbon. At high temperature, the reversible capacities of ZnP_2 and Cu_3P are only slightly increased. While for TiP_2, increasing the temperature greatly improves the performance. At 80 °C, the reversible capacity of TiP_2 was more than 3 times of that at 30 °C. Binder plays an important role in the electrochemical performance of phosphides materials. Better reversible capacity and cycle life was observed for electrodes made with PI binder than PVDF binder. The issues of poor cycling performance, low coulombic efficiency and large voltage hysteresis need to be solved for these materials to have commercial application.

CHAPTER 6   CONCLUSION AND FUTURE WORK

6.1   CONCLUSION

The lack of appropriate anode materials hinders the development of sodium ion batteries. Phosphorus and phosphorus-based materials are theoretically attractive anode materials for sodium ion batteries as they offer high theoretical capacity at low voltages. Phosphorus also has anomalously low volume expansion for sodium insertion compared to other metal alloys, which makes the theoretical volumetric capacity of phosphorus exceeds that of metallic sodium.

Tin phosphide (Sn_4P_3) was found to be an interesting material as negative electrode for sodium ion batteries with a high volumetric capacity. The reaction mechanism of Sn_4P_3 was studied using ex-situ X-ray diffraction (XRD) and Mössbauer spectroscopy. The results suggest that upon sodiation, Sn and P begin to react with sodium simultaneously, resulting in the formation of Na_3P and $Na_{0.6}Sn$, and Na_4Sn_4, phases. After further sodiation these Na-Sn phases react with more sodium and eventually form $Na_{15}Sn_4$. This provides a good example of the utility of Mössbauer spectroscopy for the investigation of the metal alloying reactions mechanism of Sn-containing compounds as anode materials in metal ion cells.

A survey of transition metal phosphides for use as negative electrodes in sodium ion batteries was conducted. Most of the materials have capacities much less than their theoretical capacities. Some of the materials show high reversible gravimetric and volumetric capacities that exceed that of hard carbon. It was also observed that binder plays an important role in this kind of materials. PI is a better choice of binder than PVDF with alloy materials in providing higher reversible capacity and better cycling performance. At high temperature, the reversible capacity was greatly improved and the hysteresis was reduced for TiP_2. While for some materials such as

Cu_3P and ZnP_2, high temperature does not have significant effect on reversible capacity. It was also found that the higher the volumetric capacity, the poorer the cycling performance for these transition metal phosphides. Issues with transition metal phosphides include high irreversible capacity, high voltage hysteresis, low coulombic efficiency and large capacity fade, which prevent these materials from commercial realization.

6.2 FUTURE WORK

In this work, the sodiation mechanism of Sn_4P_3 was studied. In order to gain sufficient mass for Mössbauer spectra, the electrodes were made very thick, compared to other regular electrodes (0.3 mm, compared to 0.1 mm.). The full sodiation capacity is achieved for these electrodes. However, the desodiaiton capacity is only half of that of a regular cell. Therefore, the study of the desodiation mechanism of Sn_4P_3 was not conducted. It may be interesting to examine the desodiation mechanism of Sn_4P_3 using Mössbauer spectra. The same fitting strategy could be used to study the desodiation mechanism of Sn_4P_3.

It was observed that while some transition metal phosphides readily react with sodium at room temperature, other transition metal phosphides only have very little first sodiation capacity. The reason for this phenomenon is unknown, possibly due to kinetics of the materials. Therefore the reaction mechanisms of transition metal phosphides need to be investigated in greater detail. Increasing operating temperature greatly improved the performance of TiP_2, which has volumetric capacity that exceeds that of hard carbon at 80 °C. It is worth further exploration to lower the cell temperature to 30 °C after cycling at 80 °C to see if the cell can maintain the improved reversible capacity and reduced hysteresis at a reduced temperature. Other bimetallic phosphides that contain phosphorus and two transition metals could also be studied.

REFERENCES

1. http://www.nissan-global.com/EN/NEWS/2015/_STORY/150624-02-e.html.

2. B. Dunn, H. Kamath, and J.-M. Tarascon, *Science*, **334**, 928 (2011).

3. http://www.teslamotors.com/en_CA/POWERWALL

4. 2015 - USGS Mineral Resources Program: Lithium
http://minerals.usgs.gov/minerals/pubs/commodity/lithium/mcs-2015-lithi.pdf

5. C. W. Kamienski, D. P. McDonald, M. W. Stark, and J. R. Papcun, *Kirk-Othmer Encyclopedia of Chemical Technology.*(2014)

6. U.S. Geological Survey, http://minerals.usgs.gov/minerals/pubs/commodity/lithium/ (2015)

7. Battery Market Development for Consumer Electronics, Automotive, and Industrial: Materials Requirements and Trends. C. Pillot, (2015).

8. R. V. Noorden, *Nature*, **507**, 26 (2014).

9. M. D. Slater, D. Kim, E. Lee, and C. S. Johnson, *Adv. Funct. Mater.*, **23**, 947 (2013).

10. D. Kundu, E. Talaie, V. Duffort, and L. F. Nazar, *Angew. Chem. Int. Ed.,* **54**, 3431 (2015).

11. N. Yabuuchi, K. Kubota, M. Dahbi, and S. Komaba, *Chem. Rev.*, **114**, 11636 (2014).

12. N. Yabuuchi, M. Kajiyama, J. Iwatate1, H. Nishikawa, S. Hitomi, R. Okuyama2, R. Usui, Y. Yamada, and S. Komaba, *Nat. Mater.*, **11**, 512 (2012).

13. N, Yabuuchi, R. Hara, K. Kubota, J. Paulsen, S. Kumakur, and S. Komaba, *J. Mater. Chem. A*, **2**, 16851 (2014).

14. X. Wang, G. Liu, T. Iwao, M. Okubo, and A. Yamada, *J. Phys. Chem. C*, **118**, 2970 (2014).

15. P. Barpanda, G. Oyama, S. Nishimura, S.-C. Chung, and A. Yamada, *Nat. Commun.*, **5**, 1 (2014).

16. M. Reynaud, G. Rousse, A. M. Abakumov, M. T. Sougrati, G. V. Tendeloo, J.-N. Chotarda, and J.-M. Tarascon., *J. Mater. Chem. A*, **2**, 2671 (2014).

17. M. Jäckle and A. Groß, *J. Chem. Phys.*, **141**, 174710 (2014).

18. D. P. Divincenzo and E. J. Mele, *Phys. Rev. B*, **32**, 2538 (1985).

19. D. A. Stevens and J. R. Dahn, *J. Electrochem. Soc.*, **147**, 1271 (2000).

20. J. Zhao, L. Zhao, K. Chihara, S. Okada, J. Yamaki, S. Matsumoto, S. Kuze, and K. NakaneJ, *J. Power Sources*, **244**, 752 (2013).

21. L. D. Ellis, T. D. Hatchard, and M. N. Obrovac, *J. Electrochem. Soc.*, **159**, A1801 (2012).

22. Y. Kim, Y. Park, A. Choi, N.-S. Choi, J. Kim, J. Lee, J. H. Ryu, S. M. Oh, and K. T. Lee, *Adv.Mater.*, **25**, 3045 (2013).

23. J. Qian, X. Wu, Y. Cao, X. Ai, and H. Yang, *Angew. Chemie. Int. Ed.*, **52**, 4633 (2013).

24. L. D. Ellis, B. N. Wilkes, T. D. Hatchard, and M. N. Obrovac, *J. Electrochem. Soc.*, **161**, A416 (2014)

25. A. Darwiche, C. Marino, M. T. Sougrati, B. Fraisse, L. Stievano, and L. Monconduit, *J. Am. Chem. Soc.*, **134**, 20805 (2012).

26. M. N. Obrovac and V. L. Chevrier, *Chem. Rev.* **114**, 11444 (2014).

27. J. Qian, Y. Xiong, Y. Cao, X. Ai, and H. Yang, *Nano Lett.*, **14**, 1865 (2014).

28. Y. Kim, Y. Kim, A. Choi, S. Woo, D. Mok, N.-S. Choi, Y. S. Jung, J. H. Ryu, S. M. Oh, and K. T. Lee, *Adv. Mater.*, **26**, 4139 (2014).

29. W.-J. Li, S.-L. Chou, J.-Z. Wang, H.-K. Liu, and S.-X. Dou, *Chem. Commun.*, **51**, 3682 (2015).

30. J. Fullenwarth, A. Darwiche, A. Soares, B. Donnadieu, and L. Monconduit, *J. Mater. Chem. A*, **2**, 2050 (2014).

31. T. Ohzuku and A. Ueda, *J. Electrochem. Soc.*, **141**, 2972 (1994).

32. Z. Lu, D. D. MacNeil, and J. R. Dahn, *Electrochem. Solid-State Lett.*, **4**, A200 (2001).

33. T. Ohzuku and Y. Makimura, *Chem. Lett.*, **30**, 642 (2001).

34. C.H. Chen, J. Liua, M.E. Stoll, G. Henriksen, D.R. Vissers, and K. Aminea, *J. Power Sources*, **128**, 278 (2004).

35. K. Hwang, S. Lee, and S. Joo, *J. Electrochem. Soc.*, **141**, 3296 (1994).

36. T. Ohzuku, M. Kitagawa, and T. Hitai, *J. Electrochem. Soc.*, **137**, 40 (1990).

37. R. Santhanam and B. Rambabu, *J. Power Sources*, **195**, 5442 (2010).

38. A. K. Padhi, K. S. Nanjundaswamy, and J. B. Goodenough, *J. Electrochem. Soc.*, **144**, 1188 (1997).

39. Yamada, S. C. Chung, and K. Hinokuma, *J. Electrochem. Soc.*, **148**, A224 (2001).

40. Z. Chen and J. R. Dahn, *J. Electrochem. Soc.*, **149**, A1184 (2002).

41. Y. Mikhaylik, I. Kovalev, R. Schock, K. Kumaresan, J. Xu, J. Affinito, *ECS Transactions*, **35,** 23 (2010).

42. J. R. Dahn, T. Zheng, Y. Liu, and J. S. Xue, *Science.*, **270**, 590 (1995).

43. M. N. Obrovac and L. Christensen, *Electrochem. Solid-State Lett.*, **7**, A93 (2004).

44. J. Yang, M. Winter, and J.O. Besenhard, *Solid State Ionics*, **90**, 281 (1996).

45. J. Park, *Principles and Applications of Lithium Secondary Batteries*, (2012).

46. S. Ahmad, *Ionics*, **15**, 309 (2009).

47. E. Peled, *J. Electrochem. Soc.*, **126**, 2047 (1979).

48. P. Verma, P. Maire, and P. Novák, *Electrochim. Acta*, **55**, 6332 (2010).

49. G. H. Newman and L. P. Klemann, *J. Electrochem. Soc.*, **127**, 2097 (1980).

50. J.-J. Braconnier, C. Delmas, C. Fouassier, and P. Hagenmuller, *Mater. Res. Bull.*, **15**, 1797 (1980).

51. M. S. Whittingham, *Prog. Solid State Chem.* **12**, 41 (1978).

52. A. S. Nagelberg, W. L. Worrell, *J. Solid State Chem.* **29**, 345 (1979).

53. M. H. Han, E. Gonzalo, G. Singh, and T. Rojo, *Energy Environ. Sci.*, **8**, 81 (2015)

54. C. Delmas, C. Fouassier, and P. Hagenmuller, *Physica B+C* , **99**, 81 (1980)

55. P. Vassilaras, X. Ma, X. Li, and G. Ceder, *J. Electrochem. Soc.*, **160**, A207 (2012)

56. N. Yabuuchi, H. Yoshida, and S. Komaba, *Electrochemistry*, **80**, 716 (2012)

57. R. Berthelot, D. Carlier, and C. Delmas, *Nat. Mater.*, **10**, 74 (2011)

58. S. Komaba, C. Takei, T. Nakayama, A. Ogata, and N. Yabuuchi, *Electrochem. commun.*, **12**, 355 (2010).

59. H. Arai, S. Okada, Y. Sakurai, and J. Yamaki, *Solid State Ionics*, **106**, 45 (1998).

60. J. Billaud, R. J. Clément, A. R. Armstrong, J. Canales-Vázquez, P. Rozier, C. P. Grey, and P. G. Bruce, *J. Am. Chem. Soc.*, **136**, 17243 (2014).

61. S. Komaba, N. Yabuuchi, T. Nakayama, A. Ogata, T. Ishikawa, and I. Nakai, *Inorg. Chem.*, **51**, 6211 (2012).

62. J. S. Thorne, R. a. Dunlap, and M. N. Obrovac, *J. Electrochem. Soc.*, **161**, A2232 (2014).

63. R. Fielden and M. N. Obrovac, *J. Electrochem. Soc.*, **162**, A453 (2015).

64. D. Hamani, M. Ati, J. M. Tarascon, and P. Rozier, *Electrochem. commun.*, **13**, 938 (2011).

65. M. Guignard, C. Didier, J. Darriet, P. Bordet, E. Elkaïm, and C. Delmas1., *Nat. Mater.*, **12**, 74 (2013).

66. D. Wu, X. Li, B, Xu, N. Twu, L. Liu, and G. Ceder, *Energy Environ. Sci.*, **8**, 195 (2015).

67. R. Fielden and M. N. Obrovac, *J. Electrochem. Soc.*, **161**, A1158 (2014).

68. D. Yuan, W. He, F. Pei, F. Wu, Y. Wu, J. Qian,Y. Cao, X. Ai, and H. Yang, *J. Mater. Chem. A*, **1**, 3895 (2013).

69. J. Billaud, G. Singh, A. R. Armstrong, E. Gonzalo, V. Roddatis, M. Armand, T. Rojo, and P. G. Bruce, *Energy Environ. Sci.*, **7**, 1387 (2014).

70. S.-M. Oh, S.-T. Myung, J. Hassoun, B. Scrosati, and Y.-K. Sun, *Electrochem. commun.*, **22**, 149 (2012).

71. P. Barpanda, G. Oyama, C. D. Ling, and A. Yamada, *Nat. commun.,* **5**, 4358 (2014).

72. B. L. Ellis, W. R. M. Makahnouk, Y. Makimura, K. Toghill, and L. F. Nazar, *Nat. Mater.*, **6**, 749 (2007).

73. K. Saravanan, C. W. Mason, A. Rudola, K. H. Wong, and P. Balaya, *Adv. Energy Mater.*, **3**, 444 (2013).

74. V. Duffort, E. Talaie, R. Black, and L. F. Nazar, *Chem. Mater.*, **27**, 2515 (2015).

75. D. A. Stevens and J. R. Dahn, *J. Electrochem. Soc.*, **148**, A803 (2001).

76. P. Thomas and D. Billaud, *Electrochim. Acta*, **47**, 3303 (2002).

77. D. A. Stevens and J. R. Dahn, *J. Electrochem. Soc.*, **147**, 4428 (2000).

78. J. R. Dahn, W. Xing, and Y. Gao, *Carbon N. Y.*, **35**, 825 (1997).

79. V. L. Chevrier and G. Ceder, *J. Electrochem. Soc.*, **158**, A1011 (2011).

80. M. Dahbi, T. Nakano, N. Yabuuchi, T. Ishikawa, K. Kubota, M. Fukunishi, S. Shibahara, J.-Y. Son, Y.-T. Cui, H. Oji, S. Komaba., *Electrochem. commun.*, **44**, 66 (2014).

81. S. Komaba, Y. Matsuura, T. Ishikawa, N. Yabuuchi, W. Murata, S. Kuze, *Electrochem. commun.*, **21**, 65 (2012).

82. S. Komaba, T. Ishikawa, N. Yabuuchi, W. Murata, A. Ito, and Y. Ohsawa, *ACS Appl. Mater. Interfaces*, **3**, 4165 (2011).

83. J. Qian, Y. Chen, L. Wu, Y. Cao, X. Ai, and H. Yang, *Chem. Commun.*, **48**, 7070 (2012).

84. J. M. Sangster, *J. Phase Equilibria Diffus.*, **31**, 62 (2010).

85. C. M. Park and H. J. Sohn, *Adv. Mater.*, **19**, 2465 (2007).

86. J. Qian, D. Qiao, X. Ai, Y. Cao, and H. Yang, *Chem. Commun.*, **48**, 8931 (2012).

87. N. Yabuuchi, Y. Matsuura, T. Ishikawa, S. Kuze, J.-Y. Son, Y.-T. Cui, H. Oji, and S. Komaba, *ChemElectroChem*, **1**, 580 (2014).

88. B. Hunter, Rietica- A Visual Rietveld Program. In International Union of Crystallography Commision on Powder Diffraction News letter No. 20; (1998).

89. H.Putz, K.Brandenburg, Match!Phase Identification from Powder Diffraction.

90. N. N. Greenwood, T. C. Gibb, Mossbauer Spectroscopy, Chapman and Hall Ltd., London, Great Britain, (1971).

91. Z. Du, R. A. Dunlap, and M. N. Obrovac, *J. Alloys Compd.*, **617**, 271 (2014).

92. J. K. Lees and P. A. Flinn, *J. Chem. Phys.*, **48**, 882 (1968).

93. R.A. Dunlap, J.S. Thorne, *J. Alloys Comp.* **577**, 278 (2013).

94. K. Lagarec and D. G. Rancourt, Recoil Mossbauer spectral analysis software for windows. (1998).

95. K. Periyapperuma, T. Tran, S. Trussler, D. Ioboni, and M. Obrovac, *J. Electrochem. Soc.*, **161**, A2182 (2014)

96. T.M. Bond, J. C. Burns, D. A. Stevens, H. M. Dahn, and J. R. Dahn, *J. Electrochem. Soc.*, **160**, A521 (2013)

97. L. Baggetto, C. A. Bridges, J.-C. Jumas, D. R. Mullins, K. J. Carroll, R. A. Meisner, E. J. Crumlin, X.

Liu, W. Yang, and G. M. Veith, *J. Mater. Chem. A*, **2**, 18959 (2014).

98. B. León, J. I. Corredor, J. L. Tirado, and C. Pérez-Vicente, *J. Electrochem. Soc.*, **153**, A1829 (2006).

99. B.N. Wilkes, Z. L. Brown, L.J. Krause, M. Triemert, and M.N. Obrovac, *submitted to J. Electrochemical Soc.*, September, 2015.

100. L. Häggström, J. Gullman, T. Ericsson, and R. Wäppling, *J. Solid State Chem.*, **13**, 204 (1975).

101. S. Woo, J.-H. Jung, H. Kim, M. G. Kim, C. K. Lee, H.-J. Sohn, and B. W. Choe, *J. Electrochem. Soc.*, **153**, A1979 (2006).

102. C. M. Park and H. J. Sohn, *Chem. Mater.*, **20**, 6319 (2008).

103. M. Bichat, T. Politova, H. Pfeiffer, F. Tancret, L. Monconduit, J.-L. Pascal, T. Brousse, and F. Favier, *J. Power Sources,* **136**, 80 (2004).

104. C. Suryanarayana, *Prog. Mater. Sci.*, **46**, 1 (2001).

105. F. Klein, B. Jache, A. Bhide, and P. Adelhelm, *Phys. Chem. Chem. Phys.*, **15**, 15876 (2013).